Chapter 25

Wave Theory, Simulation, and Determination of Gas-hydrate Content in Sediments

José M. Carcione[1], Davide Gei[1], Giuliana Rossi[1], and Umberta Tinivella[1]

Abstract

The characterization and detection of gas hydrate in sediments can be described by a Biot-type theory for wave propagation at all frequency ranges, including the effects of attenuation, partial saturation, and effective pressure. Differential equations can be recast to compute synthetic seismograms in heterogeneous media. Amplitude variations with angle (AVA) of the bottom-simulating reflector (BSR) allow one to obtain information about the concentration of gas hydrates, gas saturation, and grain cementation. Concentration and saturation can be estimated from log and VSP data and traveltime tomography, based on the Biot-Gassmann seismic-velocity equation. Moreover, the P-wave quality factor can be obtained by attenuation tomography, which constitutes an additional technique to determine the presence of hydrates, the type of fluids, and their distribution in the sediments.

Introduction

A sediment saturated with gas hydrates (clathrates) is a partially frozen porous medium in which the presence of freezing has an important effect on seismic velocities. Hence, seismic methods are suitable techniques to quantify the concentration of gas hydrates, water saturation (the unfrozen component), and gas saturation.

Leclaire et al. (1994) have proposed a theory for frozen media with three material phases (grains, ice, and water). The theory assumes no interaction between the grains and ice and predicts three compressional waves and two shear waves. Carcione and Tinivella (2000) have included the missing interaction and the effect of grain cementation as a function of ice content. The original theory of Leclaire et al. (1994) has been tested by Leclaire et al. (1995) in comparison with results obtained from laboratory experiments. Gei and Carcione (2003) further generalize the theory to include pore-pressure effects, partial saturation, and loss mechanisms of different kinds.

Carcione and Seriani (2001) develop a seismic-modeling algorithm based on the previous theory, introducing realistic seismic attenuation by using memory variables, implying additional first order in time-differential equations. The involved wave equation holds for uniform porosity. The differential equations for variable porosity are given in Biot (1962), recasting the system in terms of the matrix (or frame) displacements and variation of fluid content. Using this approach, Carcione et al. (2003) obtain the stress-strain and momentum-conservation equations of the three-phase frozen medium by using the analogy with the two-phase equations of motion and the complementary-energy theorem. On these lines, Carcione et al. (2005b) generalize the Gassmann bulk modulus (Gassmann, 1951) to model many grain minerals.

Using the above-mentioned theories, we obtain the hydrate content at the Mallik research-well location and at offshore Svalbard, Norway (Carcione and Gei, 2004; Carcione et al., 2005a). The estimation is based on seismic velocities obtained from well logs and vertical seismic profiles (VSP) in the first case and single-channel and OBS (ocean-bottom seismograph) data in the second case. The OBS data have been processed by using traveltime tomography of direct and reflected waves. The differences between the tomographic velocities and a profile for marine sediments without hydrates are converted to concentration of clathrates and saturation of free gas.

[1]Istituto Nazionale di Oceanografia e di Geofisica Sperimentale (OGS). Borgo Grotta Gigante 42/c, 34010 Sgonico, Trieste. E-mail: jcarcione@inogs.it

Differential Equations of Motion

Leclaire et al. (1994) and Carcione and Seriani (2001) deal with the constant-porosity differential equations because they are based on the average solid displacements as Lagrangian coordinates. That approach is used by Biot (1956) when he introduces for the first time the theory to model waves in a two-phase medium. Then Biot (1962) generalizes the governing equations to variable porosity using the matrix displacements and the variation of fluid content. In this case, the fluid pressure is one of the generalized forces of the Lagrangian formulation. The resulting differential equations are used to obtain synthetic seismograms in heterogeneous media. These equations are consistent with the law of Darcy and the conditions satisfied at material interfaces in porous media.

The same approach has been used by Santos et al. (1990a) and by Santos et al. (1990b) for partially saturated media. Details for a fully saturated porous medium can be found in Biot (1962) and in Carcione (2007). In the following, we describe the stress-strain relations and the momentum-conservation equations of the frozen porous medium (Carcione et al., 2003).

The notation denotes by 1, 2, and 3 the matrix, fluid, and ice (gas hydrate), respectively. Moreover, subindices $_{\rm s}$, $_{\rm f}$, and $_{\rm h}$ denote sand grains, fluids, and ice (or hydrate), respectively, and subscripts $_i$ and $_j$ refer to the spatial variables. Let us consider an elementary volume of material Ω, with Ω_m the partial volumes. The quantity of ice per unit volume of solid (grains plus ice) is denoted by I, i.e., $I = \Omega_3/(\Omega_1 + \Omega_3)$, whereas the fluid proportion is $\phi_{\rm f} = \Omega_2/\Omega = \Omega_2/(\Omega_1 + \Omega_2 + \Omega_3)$.

The following relations hold:

$$\begin{aligned}
&\phi_{\rm s} + \phi_{\rm h} + \phi_{\rm f} = 1,\\
&\phi_{\rm f} = 1 - \phi_{\rm s}/(1 - I),\\
&\phi_{\rm h} = I(1 - \phi_{\rm f}),\\
&I \;\; = \phi_{\rm h}/(\phi_{\rm s} + \phi_{\rm h}),
\end{aligned} \tag{1}$$

For a fixed proportion $\phi_{\rm s}$, the range of I is $0 < I < 1 - \phi_{\rm s}$. The ice content can be expressed alternatively as $I' = \Omega_3/(\Omega_2 + \Omega_3)$, and

$$\begin{aligned}
\phi_{\rm f} &= (1 - I')(1 - \phi_{\rm s}),\\
\phi_{\rm h} &= I'(1 - \phi_{\rm s}),
\end{aligned} \tag{2}$$

where $0 \le I' \le 1$. By *porosity*, we intend the fluid proportion ϕ_f and not the porosity when the rock has no ice, i.e., $\phi_{\rm h} + \phi_{\rm f} = 1 - \phi_{\rm s}$.

Velocity-stress formulation

The numerical algorithm uses the velocity-stress formulation of the equations of motion. These are first-order differential equations in which the field variables are the particle velocities and the stress components (see Appendix A). They can be obtained from equations A-1, A-13, A-14, and A-16 of Appendix A.

$$\begin{aligned}
\dot v_i^{(1)} &= \gamma_{11}\Pi_i^{(1)} + \gamma_{12}\Pi_i^{(2)} + \gamma_{13}\Pi_i^{(3)},\\
\dot v_i^{(3)} &= \gamma_{21}\Pi_i^{(1)} + \gamma_{22}\Pi_i^{(2)} + \gamma_{23}\Pi_i^{(3)},\\
\dot w_i &= \gamma_{31}\Pi_i^{(1)} + \gamma_{32}\Pi_i^{(2)} + \gamma_{33}\Pi_i^{(3)},
\end{aligned} \tag{3}$$

where

$$\begin{aligned}
\Pi_i^{(1)} &= \sigma_{ij,j}^{(1)} - (b_{13} + Ib_{12})(v_i^{(1)} - v_i^{(3)}) + (b_{12}/\phi_f)\dot w_i,\\
\Pi_i^{(2)} &= \sigma_{ij,j}^{(3)} - [b_{13} + (1 - I)b_{23}](v_i^{(1)} - v_i^{(3)}) + (b_{23}/\phi_f)\dot w_i,\\
\Pi_i^{(3)} &= -p_{f,i} - (\eta_w/\kappa)[\dot w_i + \phi_f(I - \kappa/\kappa_i)(v_i^{(3)} - v_i^{(1)})].
\end{aligned} \tag{4}$$

A dot above a variable indicates time differentiation, and a spatial derivative with respect to the variable x_i is denoted by subscript $_i$. Moreover, γ_{ij} are the components of

$$\begin{pmatrix}
\rho_{11} + (1 - I)\rho_{12} & \rho_{13} + I\rho_{12} & \rho_{12}/\phi_f\\
\rho_{13} + (1 - I)\rho_{23} & \rho_{33} + I\rho_{23} & \rho_{23}/\phi_f\\
\rho_{w1} & \rho_{w3} & \psi
\end{pmatrix}^{-1}, \tag{5}$$

where ψ is given by equation A-18 of Appendix A.

The stress/particle-velocity relations are obtained from equation A-36 of Appendix A and by using $\varepsilon_{ij}^{(m)} = (v_{i,j}^{(m)} + v_{i,j}^{(m)})/2$, $m = 1, 3$. The velocity-stress formulation in matrix form is

$$\dot{\mathbf{v}} = \mathbf{M}\mathbf{v} + \mathbf{s}, \tag{6}$$

where

$$\mathbf{v} = [v_i^{(1)}, v_i^{(3)}, \dot w_i, \sigma_{ij}^{(1)}, \sigma_{ij}^{(3)}, p_f]^T \tag{7}$$

has 22 variables in three dimensions and 13 variables in two dimensions,

$$\mathbf{s} = [0, 0, 0, 0, 0, 0, 0, 0, 0, 0, s_{ij}^{(1)}, s_{ij}^{(3)}, s_{ij}^{(2)}]^T \tag{8}$$

is the vector of sources, and matrix $\mathbf{M}$ is the propagation matrix.

The theory predicts five wave modes. P1 and S1 are the classic P- and S-waves, corresponding to motion in phase. These modes are waves no matter the viscosity values and frame permeabilities. Modes P2 and S2 are Biot slow P and S modes, which are waves for nil fluid viscosity and infinite permeability and quasi-static modes for finite values of viscosity and permeability. These modes propagate

(as waves) mainly in the ice frame with increasing ice content. Finally, P3 is a quasi-static mode at zero and full water saturation, which is difficult to detect in real rocks unless viscosity is nil or permeability is very high. At very low water saturations, we have the diffusion state in the case of full freezing (the P3 and S2 velocities are zero).

In the freezing process, two main events are the formation of crystals of ice (or nucleation) and their progressive growth. This phenomenon takes place first in larger pores because of surface tension, with the consequence that freezing is not uniform. This process can be represented with fractal water saturation and ice concentration (Carcione et al., 2003). In this case, mesoscopic-loss mechanisms are important at seismic frequencies (e.g., Carcione and Picotti, 2006). Numerical simulations based on this theory can be used to predict realistic wave attenuation at different frequency ranges.

Seismic Velocities and Attenuation

Frequency-dependent velocity (velocity dispersion) and wave attenuation can provide information about the type of sediment, its fluid saturation, and the pressure and temperature conditions. Therefore, it is essential to relate those properties to hydrate content, rock porosity, pore and lithostatic pressures, fluid saturation, and frequency.

Seismic velocity and attenuation depend on frequency with varying fluid saturations. At seismic (low) frequencies (relaxed regime), the fluid achieves pressure equilibration in a seismic period. Under those conditions, we can use Wood's model (or the Reuss model) to obtain the composite fluid bulk modulus, which provides results in agreement with experimental data. At high (ultrasonic) frequencies, the fluid is unrelaxed, increasing the rock velocity (e.g., Cadoret et al., 1995). This occurs because the fluids are present in patches and are mixed.

In this case, an empirical law developed by Brie et al. (1995) can be used. It gives Reuss' and Voigt's bulk moduli at seismic and ultrasonic frequencies, respectively, constituting lower and upper bounds. Wave attenuation is modeled with a constant-Q model assigned to the dry-rock moduli (e.g., Carcione et al., 2002). To define the Q values, we assume that stiff rock frames have lower attenuation than soft rock frames. We first define the Q value of the bulk modulus and then calculate the Q value of the shear modulus using that assumption.

Seismic velocities

Seismic velocity is a key property which can provide information about rock or sediment type, fluid saturation, and related pressure-temperature conditions. Carcione and Tinivella (2000) use a generalized version of the theory developed by Leclaire et al. (1994, 1995) for ice-bearing sediments to obtain the velocities of sediments partially saturated with water and gas hydrate. The solution of the corresponding dispersion equation yields a generalization of Gassmann bulk modulus (Carcione and Gei, 2004), assuming that the clathrate fills the pores with interconnection. According to Collett et al. (1999) and Katsube et al. (1999), that pattern is present in Mallik cores.

At seismic frequencies, all the phases are in the isostrain state, constituting a "closed system." Denoting with $K_{\rm hm}$ (equation A-27 of Appendix A) and $K_{\rm sm}$ the stiffness moduli of the clathrate skeleton and rock frame, the Gassmann modulus is

$$K_G = K_{\rm sm} + K_{\rm hm} + \left(1 - \frac{K_{\rm sm}}{K_{\rm s}} - \frac{K_{\rm hm}}{K_{\rm h}}\right)^2 M, \qquad (9)$$

where

$$M = \left[\left(\phi_{\rm s} - \frac{K_{\rm sm}}{K_{\rm s}}\right)\frac{1}{K_{\rm s}} + \frac{\phi}{K_{\rm w}} + \left(\phi_{\rm h} - \frac{K_{\rm hm}}{K_{\rm h}}\right)\frac{1}{K_{\rm h}}\right]^{-1}, \qquad (10)$$

where $\phi = \phi_{\rm h} + \phi_{\rm w}$ is the real porosity and $K_{\rm s}$, $K_{\rm w}$, and $K_{\rm h}$ are the bulk moduli of grains, water, and hydrate, respectively. The composite shear modulus is simply (see equations A-30 and A-31 of Appendix A)

$$\mu_{\rm m} = \mu_{\rm sm} + \mu_{\rm hm}, \qquad (11)$$

where $\mu_{\rm sm}$ and $\mu_{\rm hm}$ are the rock and ice frame moduli, respectively.

The P and S velocities can be expressed as

$$V_{\rm P} = \sqrt{\frac{K_G + 4\mu_{\rm m}/3}{\rho}} \quad \text{and} \quad V_{\rm S} = \sqrt{\frac{\mu_{\rm m}}{\rho}}, \qquad (12)$$

where

$$\rho = \phi_{\rm s}\rho_{\rm s} + \phi_{\rm w}\rho_{\rm w} + \phi_{\rm h}\rho_{\rm h} \qquad (13)$$

is the composite density, with $\rho_{\rm s}$, $\rho_{\rm h}$, and $\rho_{\rm w}$ as the densities of grains, hydrate, and water, respectively.

Comparison of the three-phase Biot theory with other theories

The hydrate concentration can be estimated on the basis of P- and S-wave velocity and attenuation anomalies, i.e., from the deviations of those properties compared with the predictions of the theoretical models.

A comparison of four rock-physics models, including that of Gei and Carcione (2003) (three-phase Biot theory), is discussed by Chand et al. (2004). The other models have been developed by Ecker et al. (1998, 2000) (three-phase effective-medium theory), Lee et al. (1996) (empirical weighted equation), and Jakobsen et al. (2000) (differential

effective-medium theory). Chand et al. (2004) obtain the velocities versus porosity, clay content, and hydrate concentration. The models predict similar velocity values, although the variations with porosity, clay content, and hydrate content have different trends.

The TPB theory includes viscoelastic and viscodynamic effects to describe the observed wave loss from seismic to ultrasonic frequencies. In addition, it predicts the velocity dispersion from low to high frequencies and the velocity and Q-factor decrease with decreasing effective pressure. The model predicts a peak dissipation factor at approximately 40% water saturation; generally, velocity increases and Q increases with increasing hydrate content.

Bottom-simulating Reflector — AVA Analysis

Amplitude-variation-with-angle (AVA) analysis determines the variation of the reflection amplitude of the seismic signal as a function of reflection angle (or receiver offset).

The analysis of bottom-simulating-reflector (BSR) amplitude variation with offset is a valid option for estimating the amount of hydrate and gas. The BSR is assumed to be the reflector produced by the transition between hydrate-bearing and free-gas-bearing sediments. Below the BSR, another important reflector is the base of the free-gas layer, the so-called BGR (e.g., Tinivella and Accaino, 2000).

In recent years, several authors have demonstrated that AVA is a useful tool to characterize the sediments across the BSR. From a theoretical point of view, Carcione and Tinivella (2000) analyze the reflection and transmission coefficients of the top and bottom of the free-gas zone, whereas Ruan and Li (2006) calculate and analyze the individual contributions from velocity, density, and Poisson's ratio to reflection coefficient of BSR through numerical calculation.

Pertaining to application to real seismic data, Tinivella and Accaino (2000) and Tinivella (2002) apply AVA analyses to seismic and ocean-bottom-seismometer (OBS) data acquired offshore the Antarctic Peninsula. Ojha and Sain (2007) perform AVA modeling of seismic-reflection data to investigate seismic velocities for quantitative assessment of gas hydrates and to understand the origin of the BSR in the western continental margin of India.

We focus our attention on the study of Carcione and Tinivella (2000) and the following application to real data sets, reporting the theoretical reflection and transmission coefficients at the BSR, by using the wave velocities from the Biot-type three-phase theory (see Appendix A of this chapter and Carcione and Tinivella, 2000) and then using a single-phase model that includes attenuation effects (e.g., Carcione, 1997). The petrophysical parameters of the sediments, hydrate, and free gas are reported in Table 1, in agreement with Carcione and Tinivella (2000). The quality factors are supposed to be equal to 30 in the hydrate layer and 20 below the BSR.

Carcione and Tinivella (2000) emphasize that the introduction of grain cementation in the Biot-type three-phase theory is evidenced by significant AVA anomaly. Figures 1 and 2 report the PP-wave theoretical reflection curves at the BSR supposing that the high hydrate saturation influences the rigidity of the solid part (Figure 1) and neglecting the cementation effects caused by hydrate presence (Figure 2). On the other hand, the free-gas presence influences only the magnitude of the PP reflection coefficient (Figures 1 and 2). Moreover, as already evidenced by several authors, the AVA curves cannot be used to estimate the free-gas concentration.

Figure 3 shows PS reflection coefficients at 25 Hz, supposing 10% of gas-hydrate saturation and various free-gas saturation (Figure 3a) and 10% of free-gas saturation and various hydrate saturations (Figure 3b). As pointed out by Carcione and Tinivella (2000), PS reflection coefficient is an indicator of large amounts of free gas and gas hydrate, even if the amplitude is lower than the PP reflection coefficients.

For completeness, we report PP reflection coefficients, phases, and interference coefficients corresponding to the BGR, supposing frequency equal to 25 Hz and both quality factors below the BGR equal to 30 (Figure 4). Also in this case, the free-gas saturation cannot be determined by the type of anomaly but only from amplitude strength, although all saturations considered in this study are characterized by the same type of anomaly. The interference between the incident and reflected P-waves (i.e., loss of energy) is particularly high for all the saturations at far incidence angles, which generally are not reached by conventional seismic surveys.

Table 1. Properties of Berea sandstone and pore infill.

Grains	Bulk modulus (K_s)	38.6 GPa
	Shear modulus (μ_s)	39.5 GPa
	Density (ρ_s)	2650 kg/m^3
Gas hydrate	Bulk modulus (K_h)	8.26 GPa
	Shear modulus (μ_h)	3.4 GPa
	Density (ρ_h)	920 kg/m^3
Water	Bulk modulus (K_w)	2.93 GPa
	Density (ρ_w)	1030 kg/m^3
Free gas	Bulk modulus (K_g)	23.6 MPa
	Density (ρ_g)	116 kg/m^3
Rock frame	Bulk modulus (K_{sm})	1.095 GPa
	Shear modulus (μ_{sm0})	1.19 GPa

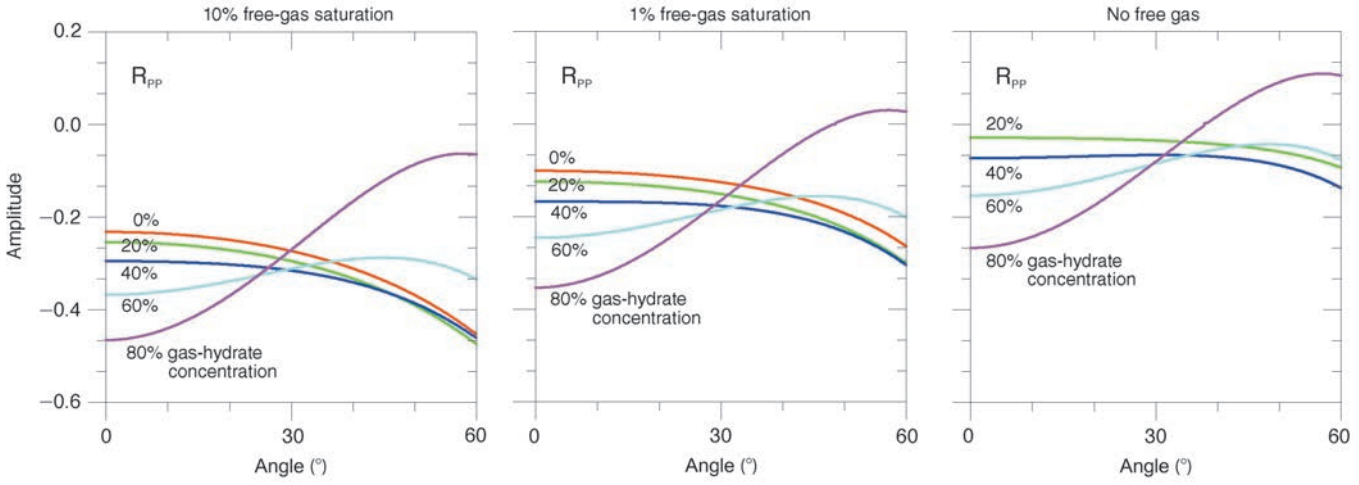

Figure 1. PP-wave viscoelastic reflection coefficient versus incidence angle and free-gas and gas-hydrate saturations (Biot-type three-phase model with grain cementation). After Carcione and Tinivella, 2000. Used by permission.

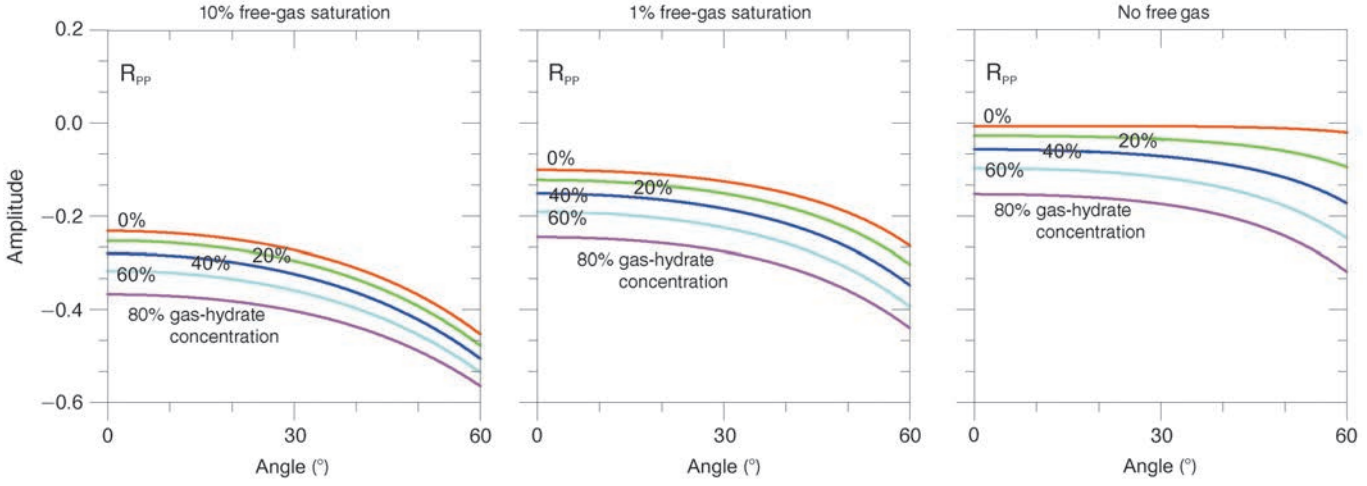

Figure 2. PP-wave viscoelastic reflection coefficient versus incidence angle and free-gas and gas-hydrate saturations (Biot-type three-phase model without grain cementation). After Carcione and Tinivella, 2000. Used by permission.

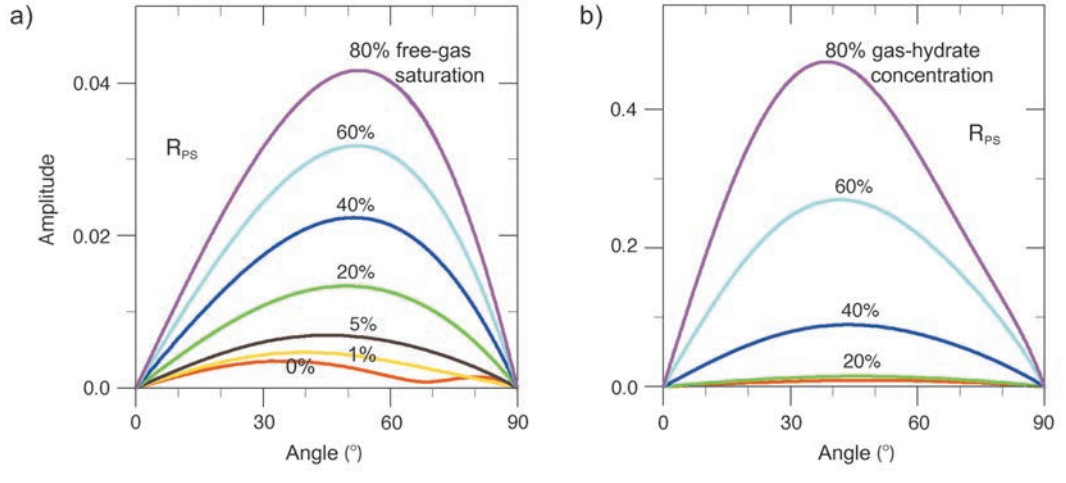

Figure 3. PS-reflection coefficients versus incidence angle for sediments with (a) 10% hydrate content and (b) 10% gas saturation (b). After Carcione and Tinivella, 2000. Used by permission.

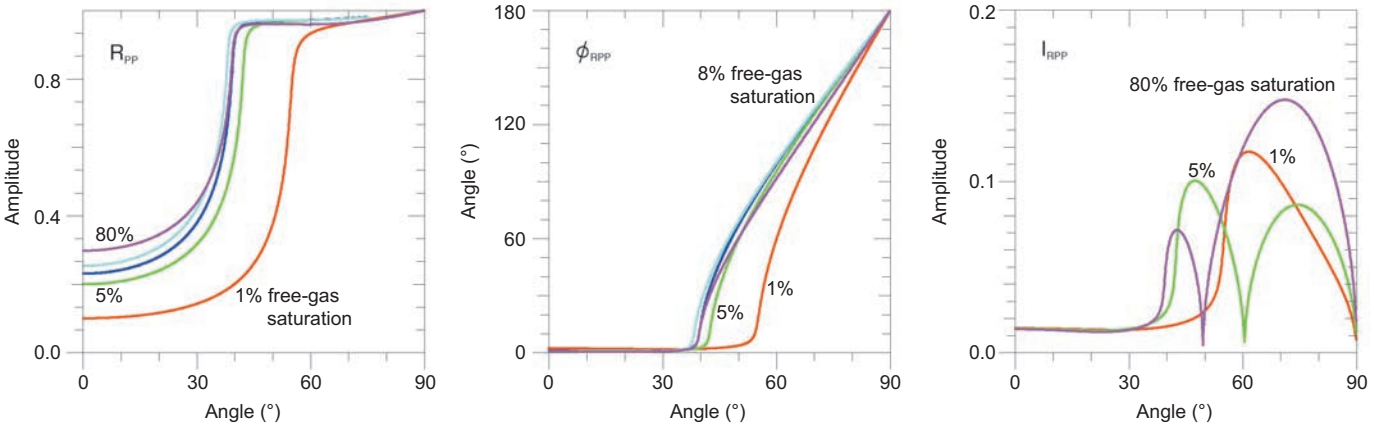

Figure 4. PP-reflection coefficients, phases, and interference coefficients versus incidence angle for the bottom of the free-gas zone. Different saturations of free gas are considered. After Carcione and Tinivella, 2000. Used by permission.

To show the application of AVA curves to real cases, we report two examples of PP and PS reflection coefficients (Tinivella and Accaino, 2000; Tinivella, 2002) extracted by seismic data acquired offshore the Antarctic Peninsula, where an important gas-hydrate reservoir is present (e.g., Tinivella et al., 2009). Several geophysical data were acquired in that area to characterize and quantify the presence of gas hydrate and free gas in the pore space: seismic (e.g., Tinivella et al., 1998; Tinivella, 1999; Tinivella and Accaino, 2000; Tinivella et al., 2002; Tinivella et al., 2009); OBS (Tinivella and Accaino, 2000; Tinivella, 2002); and chirp, gravity cores, and multibeam data (Tinivella et al., 2008; Tinivella et al., 2011).

Here we report the AVA analysis performed at water depth equal to 1780 m, where the BSR is 580 m below the seafloor in correspondence to the OBS position acquired in 1996 (Tinivella and Accaino, 2000; Tinivella, 2002). The BSR was determined by a drop in compressional velocity from 2100 m/s to 1200 m/s and a slight drop in shear velocity from 780 m/s to 730 m/s, as obtained by seismic inversion (see details in Tinivella and Accaino, 2000) (Figure 5a). In the absence of direct measurements, density was considered in agreement with Hamilton's data set (Hamilton, 1976) (Figure 5b), and compressional and shear quality factors were equal to 200 and 100, respectively, in agreement with Pecher et al. (1998).

Figure 5c indicates the PP reflection coefficients (dots) extracted at the BSR by multichannel seismic data in correspondence of the OBS position (Tinivella and Accaino, 2000). The solid line represents the theoretical curve that fits the data. As already observed by Tinivella (2002), the AVA trend indicates that the sediments in the gas-hydrate zone are not cemented. The PS reflection coefficient is reported in Figure 5d (Tinivella, 2002). The amplitude extracted from horizontal geophones of OBS data is depicted as triangles, and the best fit is indicated by a dotted line. The solid line indicates the PS theoretical curve evaluated by using the velocities and densities reported in Figure 5a and 5b. Note that the PS reflection coefficient indicates low amplitude, as expected (Tinivella, 2002).

Numerical Algorithm for Wave Propagation

Equation 6 has the following formal solution for $\mathbf{v}(0) = \mathbf{v}_0$:

$$\mathbf{v}(t) = \exp(t\mathbf{M})\mathbf{v}_0 + \int_0^t \exp(\tau\mathbf{M})s(t-\tau)d\tau. \quad (14)$$

The problem is "stiff" in mathematical terms because $\mathbf{M}$ has eigenvalues which differ by orders of magnitude resulting from the presence of the viscosity terms. To solve this problem, Carcione and Seriani (2001) introduce a splitting method based on the partition

$$\mathbf{M} = \mathbf{M}_r + \mathbf{M}_s, \quad (15)$$

where $_r$ and $_s$ denote the regular and stiff matrices, respectively. If time is $t = ndt$, where n is a natural number and dt is the time step, then the partition

$$\exp(\mathbf{M}dt) = \exp\left(\frac{1}{2}\mathbf{M}_s dt\right)\exp\left(\frac{1}{2}\mathbf{M}_r dt\right)\exp\left(\frac{1}{2}\mathbf{M}_s dt\right) \quad (16)$$

can be used to solve the stiff part independently of the regular part. If $\otimes$ denotes the product of two matrices, we have

$$\mathbf{M}_s = \begin{pmatrix} \mathbf{I}_2 \otimes \mathbf{S} & 0 \\ 0 & 0 \end{pmatrix}, \quad (17)$$

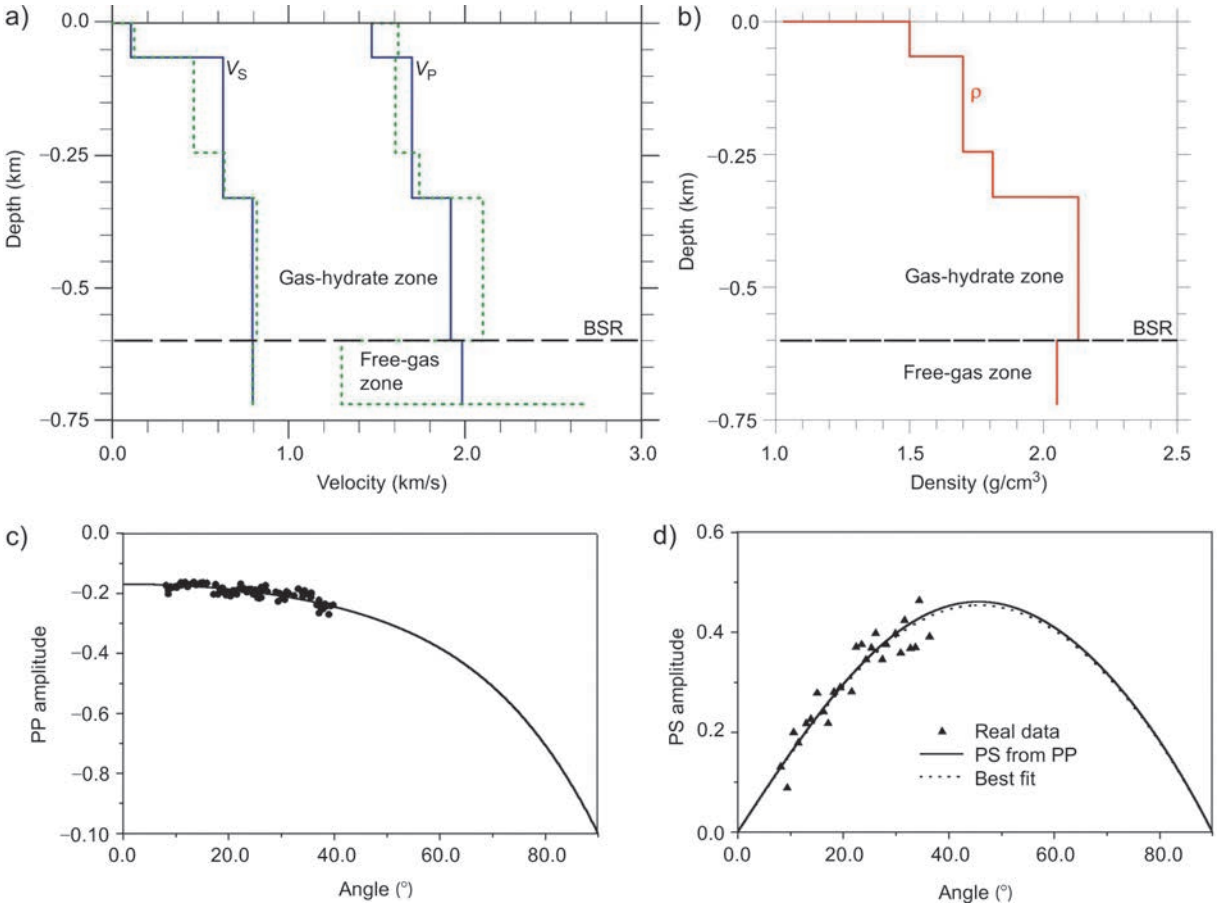

Figure 5. (a) Compressional (V_P) and shear (V_S) velocities extracted from seismic data (solid blue lines) and background velocities (dotted green lines). The depth of the BSR, indicated by the dashed black line, is in meters below the seafloor. After Tinivella and Accaino, 2000. Used by permission. (b) Density (ρ) versus meters below sea level evaluated supposing 9% of gas hydrate above the BSR (indicated with a dashed black line) and 2% of free gas below it. After Tinivella and Accaino, 2000. Used by permission. (c) PP reflection coefficient at the BSR. Dots represent amplitude extracted from multichannel seismic data. The solid line represents a theoretical curve that fitted the data. After Tinivella, 2002. Used by permission. (d) PS reflection coefficient at the BSR. Triangles represent amplitude extracted from OBS data. The dotted line represents a theoretical curve that fitted the real data. The solid line represents the theoretical reflection coefficient obtained by using the results of seismic inversion. After Tinivella, 2002. Used by permission.

with $\mathbf{I}_2$ being the identity matrix of dimension 2 (here we have assumed a 2D medium). We have to solve

$$\dot{\mathbf{w}}_i = \mathbf{S}\mathbf{w}_i \tag{18}$$

for each spatial variable with subindex $_i$, where

$$\mathbf{w}_i = [v_i^{(1)}, v_i^{(3)}, w_i]^{\mathrm{T}} \tag{19}$$

and

$$\begin{aligned}
S_{11} &= a\gamma_{11} + c\gamma_{12} + [Ib - (1 - I)d]\gamma_{13},\\
S_{12} &= -S_{11},\\
S_{13} &= b\gamma_{11} + d\gamma_{12} - [(b + d)/\phi_w]\gamma_{13},\\
S_{21} &= a\gamma_{21} + c\gamma_{22} + [Ib - (1 - I)d]\gamma_{23},\\
S_{22} &= -S_{21},\\
S_{23} &= b\gamma_{21} + d\gamma_{22} - [(b + d)/\phi_w]\gamma_{23},\\
S_{31} &= a\gamma_{31} + c\gamma_{32} + [Ib - (1 - I)d]\gamma_{33},\\
S_{32} &= -S_{31},\\
S_{33} &= b\gamma_{31} + d\gamma_{32} - [(b + d)/\phi_w]\gamma_{33},
\end{aligned} \tag{20}$$

where

$$\begin{aligned}
a &= -(b_{13} + Ib_{12}),\ b = b_{12}/\phi_w,\\
c &= b_{13} + (1 - I)\, b_{23},\ d = b_{23}/\phi_w,
\end{aligned} \tag{21}$$

with b_{ij} being friction coefficients (see equations A-2 of Appendix A).

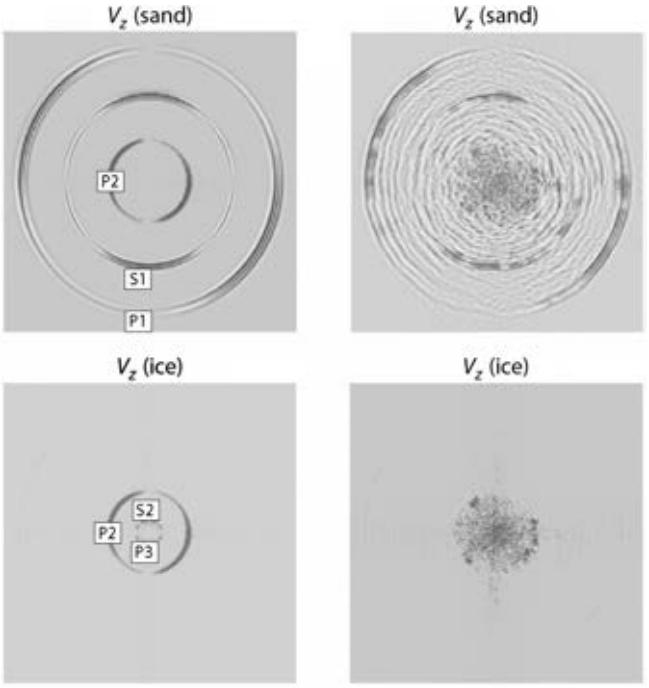

Figure 6. Snapshots of the vertical particle-velocity field propagating in the rock frame at 37 μs. P1, P2, and P3 are compressional waves, and S1 and S2 are shear waves. After Carcione et al., 2003. Used by permission.

One eigenvalue of **S** is nil, and the other eigenvalues are

$$\lambda_1 = \frac{1}{2}[\mathrm{tr}(\mathbf{S}) - \sqrt{4(S_{13} - S_{23})S_{31} + (S_{21} + S_{33} - S_{11})^2}],$$
$$\lambda_2 = \mathrm{tr}(\mathbf{S}) - \lambda_1. \tag{22}$$

We use a Runge-Kutta fourth-order time-stepping algorithm and the Fourier method to calculate the spatial derivatives (e.g., Carcione, 2007). Carcione and Helle (1999) have solved the same problem for a two-phase medium.

Figure 6 shows snapshots in a sandstone where ice distribution is fractal (the average diameter of the ice accumulations is 1 mm). We consider a mesh with 357 × 357 points, with the source located at (178, 178), and we assume an ideal fluid (zero viscosity). The slow modes P2, P3, and S2 propagate mainly in the ice, with scattering and conversion occurring at the heterogeneities.

Velocity and Attenuation Tomographic Inversion

In the absence of direct measurements such as well-log data, seismic properties are essential for a quantitative estimation of hydrate content and gas saturation. Seismic tomography is a technique that provides a reliable velocity field versus depth. In fact, traveltime seismic tomography, compared with conventional seismic-velocity analysis (stacking), can consider complex geometric models and lateral velocity variations (Böhm et al., 1997). Another advantage compared with the traditional approach is the possibility of using all the events — reflected, refracted, and direct waves (Vesnaver, 1996). Moreover, we can invert P-, S-, and PS converted waves, creating a multiparameter model (Rossi and Vesnaver, 2001; Böhm et al., 2002). If the pulse frequency content is analyzed, other properties such as attenuation can be obtained, adding new information for a more complete and correct interpretation.

Traveltime seismic tomography is based on a relation between traveltime and seismic velocity through a line integral along the raypath. The tomographic inversion consists of minimizing the difference (Δt) between the experimental (observed) time (t^{obs}) and the calculated time (t^{calc}), using seismic velocity as a parameter.

The main equation of the tomographic method is equation 23, where the line integral has been substituted by a summation over the $_j$ voxels because usually a discrete blocky model is adopted: Δs is therefore the ray segment in the voxel, and Δu is the slowness ($u = 1/V$):

$$\Delta t = t^{\mathrm{obs}} - t^{\mathrm{calc}} = \sum_j \Delta s_j \Delta u_j. \tag{23}$$

The velocity generally is assumed to be constant within the voxels, and the voxels might be based on regular or irregular gridding. The latter has the advantage that it can be denser where there is more information or when velocities change rapidly, and it can be coarser where there are fewer data or velocities are constant (Böhm et al., 1997). The staggering procedure, which averages the tomographic field obtained from coarse, slightly staggered grids, enables us to achieve a higher resolution (Vesnaver and Böhm, 2000).

When dealing with reflected or refracted waves, the shape and position of the reflecting/refracting surfaces that constitute the base and top of the voxels are obtained through an iterative process based on the principle of minimal dispersion and assuming continuity of the geologic interfaces (Rossi et al., 2001). Because of the attenuation, high frequencies are lost and pulse broadening occurs. Time rise or the spectral frequency shift is used to quantify the phenomenon (Zucca et al., 1994; Quan and Harris, 1997). The frequency analysis seems to be more robust compared with those of methods based on amplitude decay because the frequency shift is not affected by geometric spreading and mode conversion at material interfaces. A test of the robustness of this approach can be found in Picotti and Carcione (2006).

In particular, a relationship similar to equation 23 relates the spectral frequency shift (ξ) and attenuation α. It follows that

$$\Delta \xi = \xi^{\mathrm{obs}} - \xi^{\mathrm{calc}} = \sum_j \Delta s_j \Delta \alpha_{0j}, \tag{24}$$

where Δs is the ray segment and $\Delta\alpha_0$ is the attenuation factor in the voxel. We note that α_0 is α/f where f is frequency, and

$$\alpha_0 = [\pi/(QV)], \tag{25}$$

approximately, where Q is the quality factor and V is the seismic velocity.

The spectral frequency shift is given by equation 27 below, where f_s and f_r are the spectral centroids of the signal at the source and receiver, respectively. For instance,

$$f_s = \int_0^\infty \frac{fA_s(f)df}{A_s(f)df}, \tag{26}$$

where $A_s(f)$ is the amplitude spectrum of the wavelet at the source. If σ_s^2 is the spectral variance of the signal at the source (Quan and Harris, 1997),

$$\xi = \frac{f_s - f_r}{\sigma_s^2}. \tag{27}$$

The technique is therefore relatively simple and fast because the picked traveltimes can be used as a reference for frequency analysis, to provide information on the attenuation of the same events analyzed to obtain seismic velocities. For a more detailed description of the method to estimate the spectral centroid shift and the attenuation tomographic inversion, see Rossi et al. (2007).

Estimation of Gas-hydrate Concentration

The differences between the velocity profile obtained from data and the theoretical velocity in the absence of hydrates are used to quantify the hydrate and free-gas content. Positive anomalies indicate the presence of hydrates and negative anomalies the presence of free gas.

Mallik well at the Mackenzie Delta

The Mallik research borehole in the Canadian Arctic has been drilled to detect gas hydrates in permafrost. Figure 7 shows its location in the Mackenzie Delta. The stratigraphic column consists of 1150 m of sandstones containing silt/clay layers. The permafrost is located in the upper part (640 m). The study includes permafrost and gas-hydrate coring, downhole well logging, and an electromagnetic survey. The data are a VSP survey using multicomponent receivers and multipolarized vibrator sources (Walia et al., 1999). The gas hydrates are located between depths of 897 m and 1110 m. The sediments below the gas-hydrate zone are saturated with water (Miyairi et al., 1999).

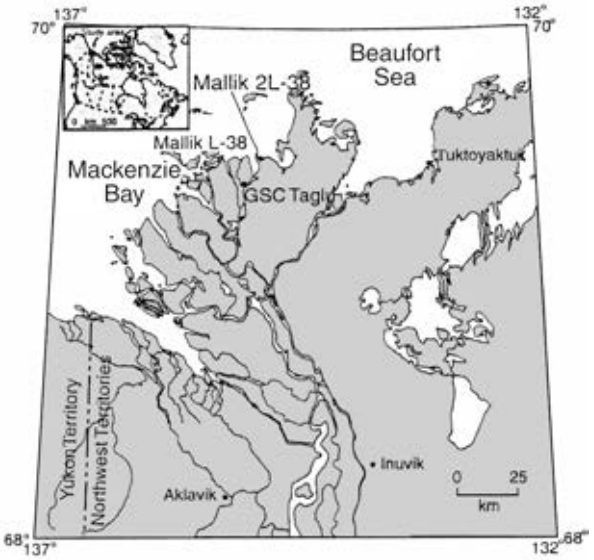

Figure 7. Location of the Mallik research well. After Miyairi et al., 1999. Used by permission.

Table 2. Material properties of permafrost at Mallik 2L-38 research well.

Quartz[2]	Bulk modulus (K_q)	36 GPa
	Shear modulus (μ_p)	45 GPa
	Density (ρ_q)	2650 kg/m^3
Clay[2]	Bulk modulus (K_c)	20.9 GPa
	Shear modulus (μ_c)	6.8 GPa
	Density (ρ_c)	2580 kg/m^3
Gas hydrate[2]	Bulk modulus (K_h)	7.7 GPa
	Shear modulus (μ_h)	3.2 GPa
	Density (ρ_h)	900 kg/m^3
Water	Bulk modulus (K_w)	2.3 GPa
	Density (ρ_w)	1030 kg/m^3

[2]Helgerud et al. (1999).

Here we consider the seismic (low-frequency) limit of the three-phase theory and neglect seismic loss. Table 2 shows the properties of the single constituents (porosity is derived from the density log from regions fully saturated with water). The well logs are averaged using a 15-m window for comparison with velocities obtained from the VSP.

Figure 8 shows the various log profiles along with P- and S-wave VSP velocities and estimated hydrate content. Shear velocities are not realistic between 900 m and 950 m, where the discrepancies with log velocities are large (this difference cannot be described with anelasticity [velocity dispersion]). We obtain average hydrate-content values of 37% and 60% from the VSP and 21% and 57% from the log velocities (from P- and S-waves, respectively). The

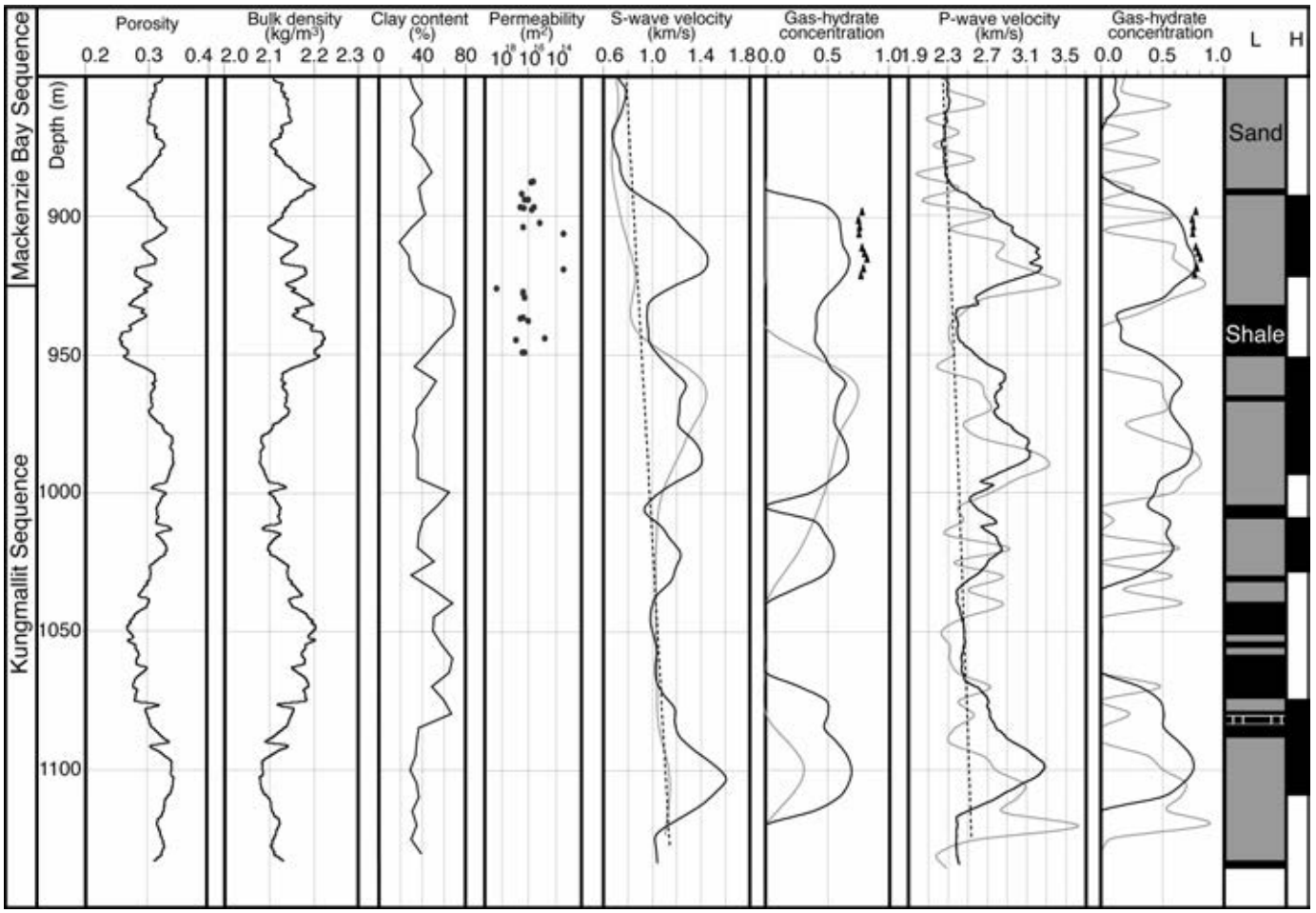

Figure 8. Log profiles and compressional- and shear-wave velocities obtained from VSP data (Mallik borehole). In the velocity panels, sonic-log measurements are shown by black curves and VSP measurements by gray curves. Velocities for full-water saturation obtained from logs are depicted by dashed lines. In column H, black intervals indicate sediments saturated with gas hydrates. Column L gives a lithologic characterization of the study depth interval, with sandstone shown in gray and shaley sandstones in black. Triangles correspond to values estimated from dissociation modeling. After Carcione and Gei, 2004. Used by permission.

plot also shows discrete concentrations obtained by Wright et al. (1999) from dissociation methods (triangles), which are higher than our results. However, the latter agree with values calculated from the Archie equation (Guerin and Goldberg, 2002). More details can be found in Carcione and Gei (2004).

Norwegian-Svalbard continental margin

The study area is the Knipovich Ridge (Lundin and Doré, 2002) (Figure 9). Upward gas flow explains the presence of hydrates and a BSR at approximately 150 m below the ocean bottom (Vanneste et al., 2002). According to Brown (1990), the combined action of geopressured gas and tectonism is the possible cause of mud diapirs.

The data consist of single-channel seismic and OBS data. The BSR reflection event has the typical characteristics of the presence of free gas, i.e., polarity reversal, high amplitude, and low frequencies (Figure 10). The profiles in Figure 10 are shown as thick lines in Figure 9. A BSR is evident at approximately 200 m below the seafloor.

The OBS data have been processed with travel-time reflection tomography to obtain the P-wave velocity (Westbrook et al., 2005; Westbrook et al., 2008). Ten P-wave reflections events were considered, four above the BSR and six below. In addition, PS-converted wave events were picked and are clearly visible in the horizontal components. Because of the different raypaths, the S-wave velocity cube coincides with the central part of the P-wave cube (Rossi et al., 2005; Westbrook et al., 2005; Westbrook et al., 2008). We can see the anomalies caused by the presence of hydrate. On the other hand, S-wave velocity increases with depth with no marked anomalies. Figure 11 shows two vertical sections of compressional velocity (see Figure 10).

As before, to estimate the gas-hydrate content, we consider the Biot-type three-phase theory. We use ODP well 986 to calibrate the model (Figure 9) (Jansen et al., 1996). The temperature gradient is 100°C/km (Vanneste

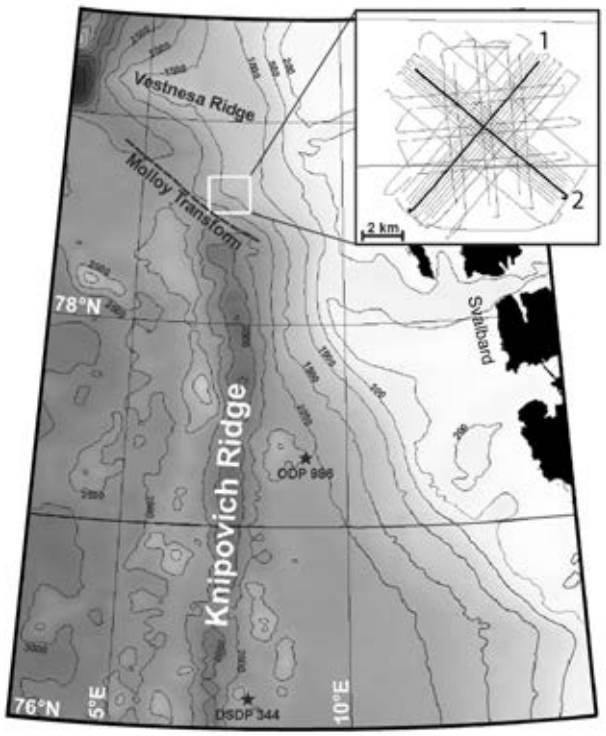

Figure 9. Bathymetry of the study area. Thick perpendicular lines correspond to the seismic profiles used in this work. After Vanneste et al., 2002. Used by permission.

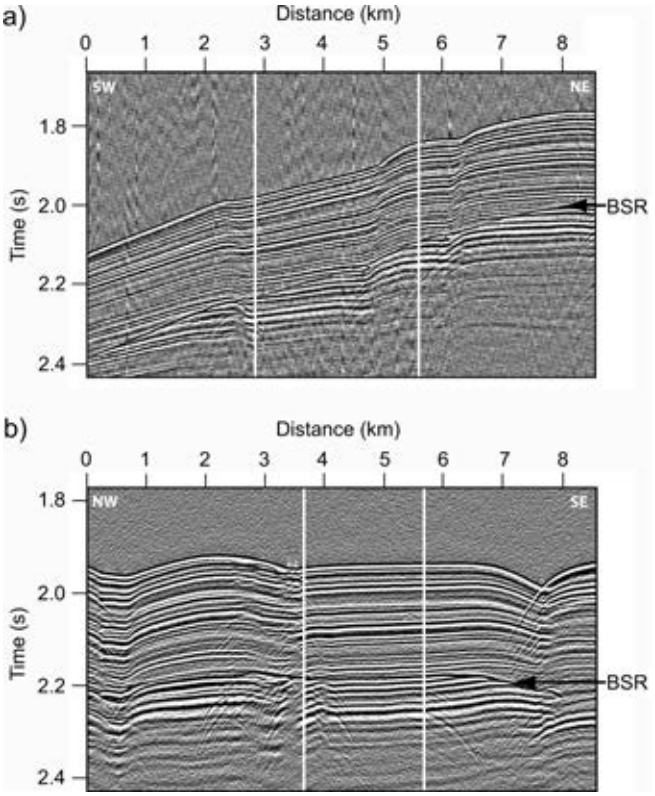

Figure 10. Seismic profiles (a) 1 and (b) 2 shown in Figure 9. Black arrows indicate the BSR. Beneath this reflection, seismic data are characterized by a lower-frequency content. The white vertical lines evidence the parts analyzed in Figures 11, 13, and 14. After Carcione et al., 2005a. Used by permission.

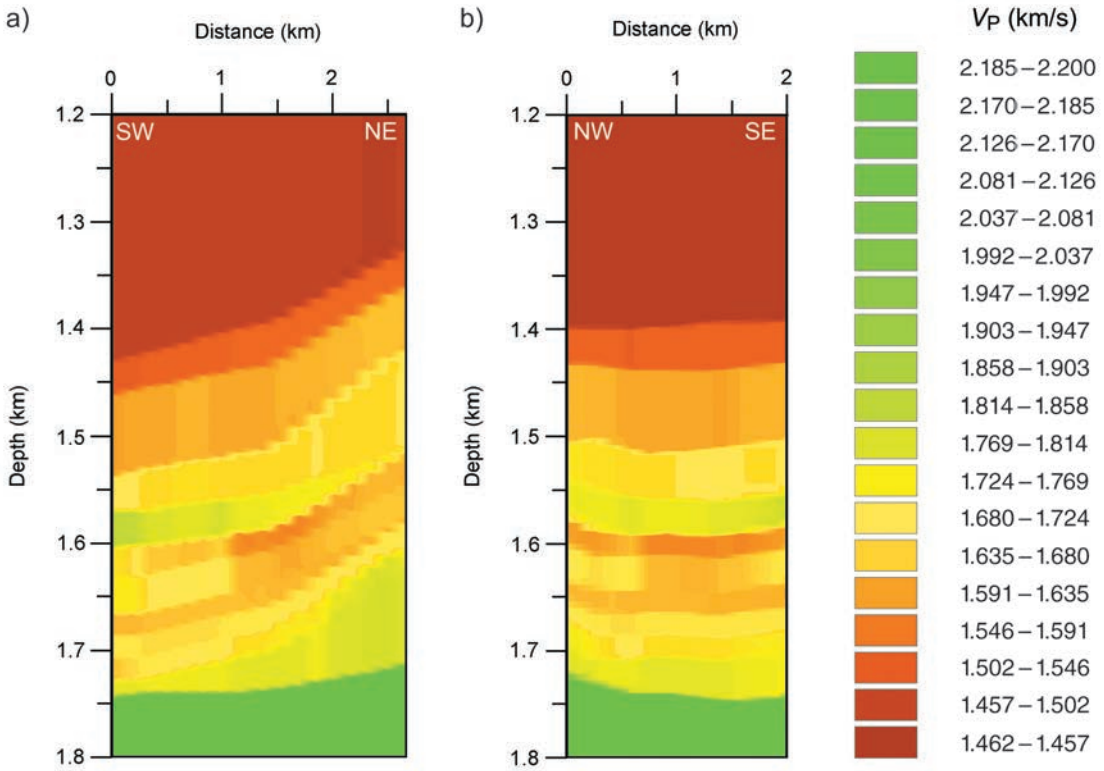

Figure 11. P-wave velocity sections obtained from seismic tomography, corresponding to the seismic sections shown in Figure 10. After Carcione et al., 2005a. Used by permission.

et al., 2005), used to obtain the properties of free gas from the equation of state (Gei and Carcione, 2003). Using core information, we consider that the grains are a mixture of quartz, calcite, and clay. Table 3 shows the properties of the single constituents. The porosity value of 45% has been obtained from Jansen et al. (1996), Figure 25.

In Figure 12, we compare the P-wave velocity computed from seismic tomography (solid line), the velocity profile at 100% water saturation (dashed line), and an empirical reference velocity (Hamilton, 1979) (dotted line), at the crossing between seismic lines 1 and 2 of Figure 9. The dashed line is obtained by inversion in an area where there is no BSR. The BSR is located at a depth of approximately 1.6 km, where compressional seismic velocity has an abrupt decrease.

Figure 13 displays vertical sections of hydrate content (blue) and gas saturation (red). The maximum values

Table 3. Material properties of the sediments at the Norwegian-Svalbard continental margin.

Grains	Bulk modulus (K_s)	29.8 GPa
	Shear modulus (μ_s)	18.0 GPa
	Density (ρ_s)	2623 kg/m^3
Gas hydrate	Bulk modulus (K_h)	7.7 GPa
	Shear modulus (μ_h)	3.2 GPa
	Density (ρ_h)	910 kg/m^3
Water	Bulk modulus (K_w)	2.24 GPa
	Density (ρ_w)	1030 kg/m^3
Free gas	Bulk modulus (K_g)	21 MPa
	Density (ρ_g)	130 kg/m^3

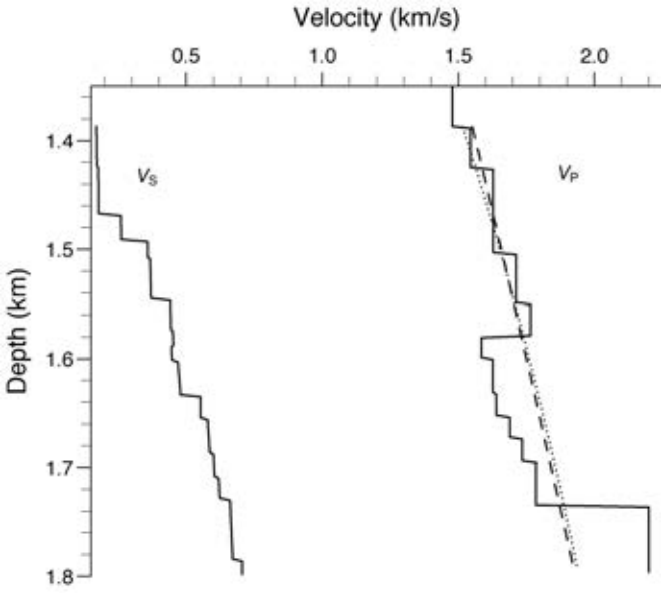

Figure 12. Solid lines represent tomographic velocity, the dashed curve references velocity, and the dotted curve represents the Hamilton velocity profile (Hamilton, 1979) at the crossing between the seismic sections shown in Figure 9. After Carcione et al., 2005a. Used by permission.

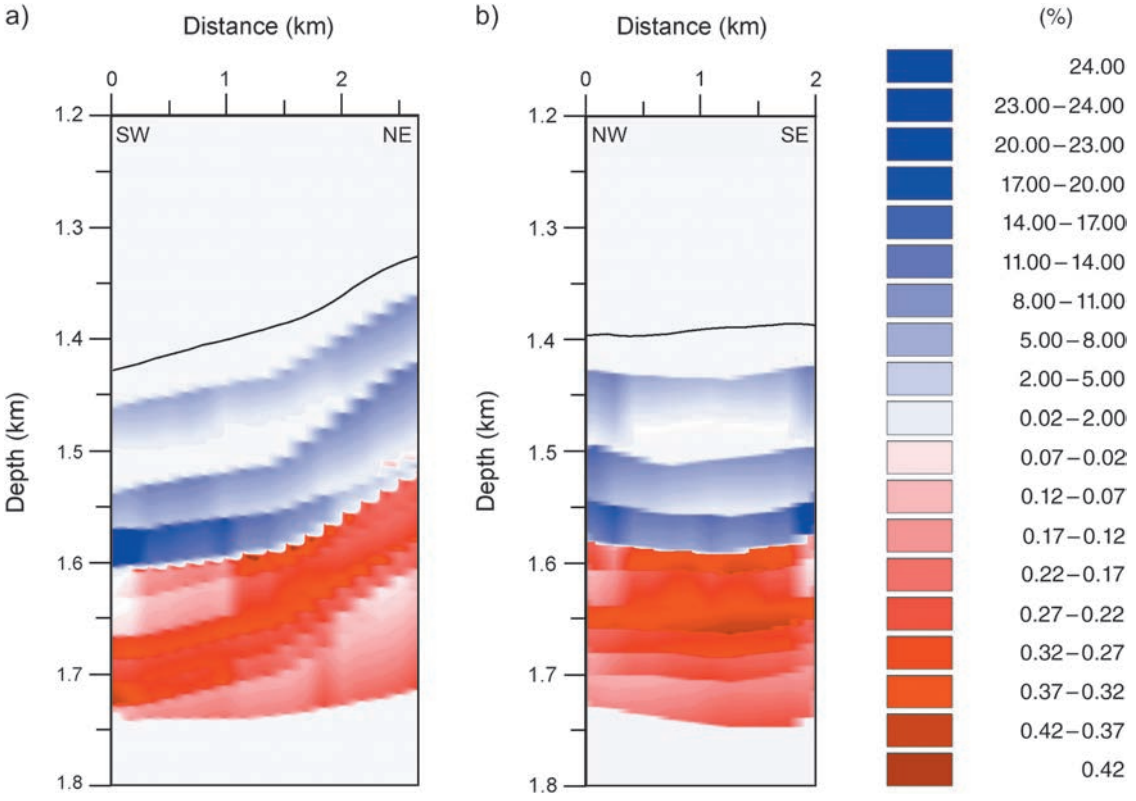

Figure 13. Vertical sections of hydrate content (blue) and gas saturation (red) (see Figure 11). Solid lines represent the seafloor. After Carcione et al., 2005a. Used by permission.

of hydrate content and gas saturation are 25% and 0.42%, with average values of 7.2% and 0.16%, respectively. The highest hydrate concentration occurs near the BSR. Bünz and Mienert (2004) obtain similar results. The results in Figure 13 correspond to the Reuss model; while using Hill's model (patchy saturation), we obtain a maximum gas saturation of 10%.

Figure 14 shows the Q_P section, and Figure 15 displays vertical profiles taken from the Q_P and Q_S cubes. The Q_P decreases below the BSR, where there is free gas, and shows high values above the BSR, where hydrate is present. On the other hand, Q_S has no significant variations. The Q_P and V_P variations agree qualitatively, indicating that both inverted values are consistent. The Q_P values agree with the data in Wood et al. (2000) and are consistent with grain cementation (Gei and Carcione, 2003).

However, there is a controversy about the relation between gas-hydrate content and wave attenuation (see, e.g., Lee, 2006). An increase in attenuation in gas-hydrate-bearing sediments is supported by sonic waveforms (Guerin and Goldberg, 2002, 2005; Matsushima, 2006) and by laboratory experiments (Priest et al., 2006), whereas the VSP and OBS data (e.g., Wood et al., 2000; Matsushima, 2006; Lee, 2006) show opposite results. More details can be found in Carcione et al. (2005a), Rossi et al. (2005), and Rossi et al. (2007).

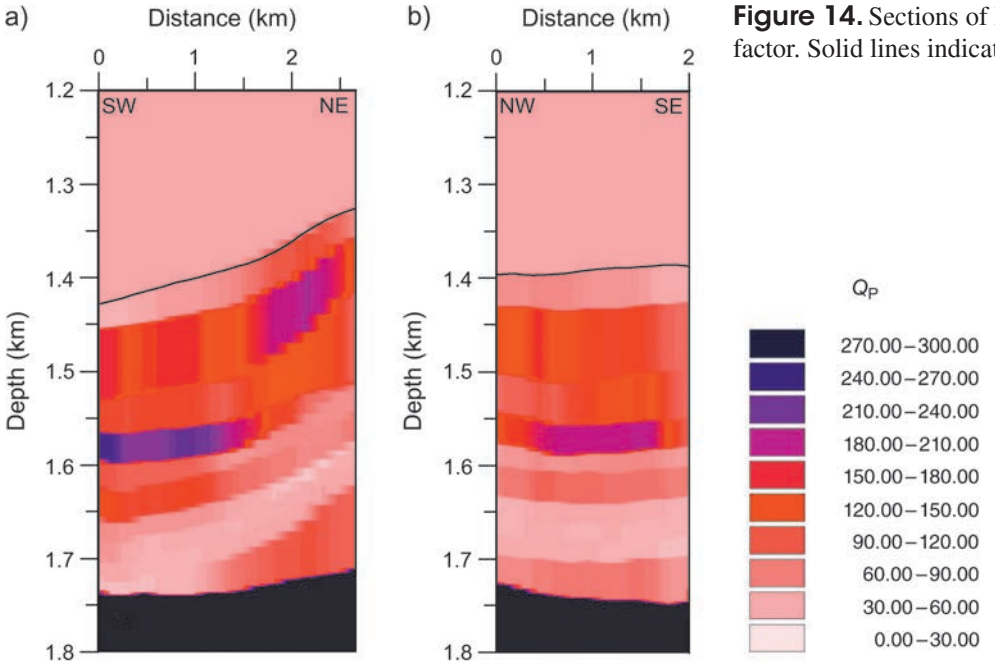

Figure 14. Sections of P-wave quality factor. Solid lines indicate the seafloor.

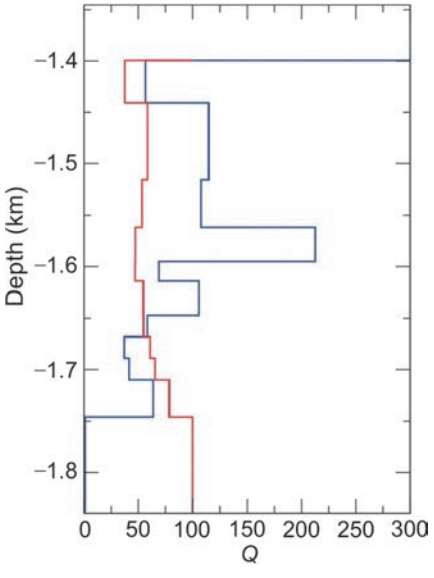

Figure 15. Vertical Q profiles extracted from P-wave (blue) and S-wave (red) cubes, respectively, at the intersection of seismic lines 1 and 2 in Figure 9.

Conclusions

The methodology to detect gas hydrates is based on seismic waves. The rock-physics model is used for a petrophysical characterization of the seismic velocities obtained from well logs and surface data and provides the equation of motion for computing seismograms in heterogeneous media at all frequency ranges. It includes the effects of attenuation, partial saturation, and effective pressure. The model is compatible with the Biot/Gassmann theory and predicts additional (slow) modes, which can be the cause of mesoscopic loss, i.e., the P-wave attenuation at seismic frequencies.

We report the main conclusion that Carcione and Tinivella (2000) drew from the AVA analysis. First of all, it is important to recall that grain cementation, simulated with a percolation model, is important for high concentrations of hydrate. As is well known, small quantities of gas in the pore space cause a dramatic drop of the compressional wave and consequently an increase in magnitude of the near-offset reflection coefficient. The AVA trend is not affected by free-gas saturation, and for low gas-hydrate concentrations, the AVA anomaly is positive. On the contrary, for high gas-hydrate concentrations, the AVA anomaly is negative.

In general, it is possible to evaluate the amount of gas hydrate or free gas by the reflection amplitude, and cementation can be determined from the trend of AVA curves. Moreover, the PS-wave amplitude increases with increasing free-gas and gas-hydrate saturations.

The gas-hydrate concentration at the Mallik research well yields average hydrate-content values of 37% and 60% from VSP and 21% and 57% from log velocities (from P-and S-waves, respectively). In the absence of log and VSP data, seismic velocity can be obtained by reflection tomography of reflected P-waves and converted PS-waves. At the western Svalbard margin, maximum hydrate contents and gas saturations of 25% and 0.42% (the Reuss model) were estimated. A value of 9% gas saturation has been obtained from Hill's model. Moreover, the P-wave quality factor obtained by attenuation tomography indicates that the presence of hydrates implies higher-quality factors compared with full water saturation.

Appendix A
Equations of Motion

The theory is given in detail in Carcione et al. (2003), Carcione and Seriani (2001), and Gei and Carcione (2003). Here we present a comprehensive summary for completeness.

Conservation of momentum

Lagrange's equations provide the momentum-conservation equations,

$$\begin{aligned}
\sigma^{(1)}_{ij,j} &= \rho_{11}\dot{v}^{(1)}_i + \rho_{12}\dot{v}^{(2)}_i + \rho_{13}\dot{v}^{(3)}_i - b_{12}(v^{(2)}_i - v^{(1)}_i) \\
&\quad - b_{13}(v^{(3)}_i - v^{(1)}_i), \\
\sigma^{(2)}_{ij,j} &= \rho_{12}\dot{v}^{(1)}_i + \rho_{22}\dot{v}^{(2)}_i + \rho_{23}\dot{v}^{(3)}_i + b_{12}(v^{(2)}_i - v^{(1)}_i) \\
&\quad + b_{23}(v^{(2)}_i - v^{(3)}_i), \\
\sigma^{(3)}_{ij,j} &= \rho_{13}\dot{v}^{(1)}_i + \rho_{23}\dot{v}^{(2)}_i + \rho_{33}\dot{v}^{(3)}_i - b_{23}(v^{(2)}_i - v^{(3)}_i) \\
&\quad + b_{13}(v^{(3)}_i - v^{(1)}_i)
\end{aligned} \tag{A-1}$$

(Leclaire et al., 1994), where subscripts $_{i,j} = 1\ (x), 2\ (y), 3\ (z)$ denote spatial coordinates, σ are the component of the stress tensor, v are the components of the particle-velocity vector, ρ are density coefficients, and b are loss parameters. Superscripts ^{1,2,3} indicate grains, fluid, and ice, respectively, and a dot above a variable indicates a time derivate, whereas subscript $_i$ denotes a spatial derivative with respect to x_i. The loss parameters are given by

$$\begin{aligned}
b_{12} &= \eta_f \phi_f^2/\kappa_s, \\
b_{23} &= \eta_f \phi_f^2/\kappa_h, \\
b_{13} &= 0,
\end{aligned} \tag{A-2}$$

where η_f is fluid viscosity, ϕ_f is fluid proportion, and κ_s and κ_h are permeabilities of the sediment and hydrate matrices, whose expressions are

$$\begin{aligned}
\kappa_s &= \kappa_{s0}\phi_f^3(1-\phi_s)^3, \\
\kappa_h &= \kappa_{h0}[(1-\phi_s)/\phi_i]^2(\phi_f/\phi_s)^3,
\end{aligned} \tag{A-3}$$

where κ_{s0} and κ_{h0} are reference values. In equation A-2, b_{13} is zero because we assume no friction between the rock and ice frame.

High-frequency viscodynamic effects are described by

$$b_{jj} = \left[\frac{\eta_f \phi_f^2}{\kappa_j}\right] F_j(\omega), \quad j = 1, 3, \tag{A-4}$$

where F_1 and F_3 describe the inelastic interaction between the fluid and the sediment and hydrate frames, $\kappa_1 = \kappa_s$, and $\kappa_3 = \kappa_h$ (Biot, 1962). It is (Johnson et al., 1987; Carcione, 2007)

$$F_j(\omega) = \sqrt{1 - \frac{4iT_j^2\kappa_j}{x_j L_j^2 \phi_f}}, \quad x_j = \frac{\eta_f \phi_f}{\omega \kappa_j \rho_f}, \quad j = 1, 3, \tag{A-5}$$

where $2/L_j$ is the ratio between the surface and volume of the pores; T_1 and T_3 are the tortuosities of the sediment and hydrate frames, respectively; ω is the angular frequency; and ρ_f is the density of the fluid. The following relation holds:

$$\xi_j T_j \kappa_j / \phi_f L_j^2 = 1, \tag{A-6}$$

where $\xi_j = 12$ and 8 for canted slabs and nonintersecting canted tubes, respectively.

The density components are

$$\begin{aligned}
\rho_{11} &= \phi_s \rho_s a_{13} + (a_{21} - 1)\phi_f \rho_f + (a_{31} - 1)\phi_h \rho_h,\\
\rho_{12} &= -(a_{21} - 1)\phi_f \rho_f,\\
\rho_{13} &= -(a_{13} - 1)\phi_s \rho_s - (a_{31} - 1)\phi_h \rho_h,\\
\rho_{22} &= (a_{21} + a_{23} - 1)\phi_f \rho_f,\\
\rho_{23} &= -(a_{23} - 1)\phi_f \rho_f,\\
\rho_{33} &= \phi_h \rho_h a_{31} + (a_{23} - 1)\phi_f \rho_f + (a_{13} - 1)\phi_s \rho_s,
\end{aligned} \tag{A-7}$$

where ρ_s and ρ_h are grain and ice densities, respectively.

Leclaire et al. (1994) found that

$$a_{21} = \left(\frac{\phi_s \rho}{\phi_f \rho_f}\right) r_{21} + 1,\ a_{23} = \left(\frac{\phi_s \rho'}{\phi_f \rho_f}\right) r_{23} + 1, \tag{A-8}$$

where

$$\rho = \frac{\phi_f \rho_f + \phi_h \rho_h}{\phi_f + \phi_h},\ \rho' = \frac{\phi_f \rho_f + \phi_s \rho_s}{\phi_f + \phi_s}, \tag{A-9}$$

and r_{21} and r_{23} are 0.5 for spheres (Berryman, 1980). Equivalently, we assume

$$a_{13} = \left(\frac{\phi_s \rho''}{\phi_s \rho_s}\right) r_{13} + 1,\ a_{31} = \left(\frac{\phi_s \rho''}{\phi_h \rho_h}\right) r_{31} + 1, \tag{A-10}$$

where

$$\rho'' = \frac{\phi_h \rho_h + \phi_s \rho_s}{\phi_h + \phi_s}. \tag{A-11}$$

The fluid displacement relative to the frames is

$$w_i = \phi_f [u_i^{(2)} - (1 - I)u_i^{(1)} - I u_i^{(3)}], \tag{A-12}$$

where u denotes displacements $(v = \dot{u})$ and I is ice content. Substituting equation A-12 into A-1, we obtain

$$\begin{aligned}
\sigma_{ij,j}^{(1)} = {} & [\rho_{11} + (1 - I)\rho_{12}]\dot{v}_i^{(1)} + (\rho_{13} + I\rho_{12})\dot{v}_i^{(3)}\\
& + (\rho_{12}/\phi_f)\ddot{w}_i + (b_{13} + I b_{12})(\dot{v}_i^{(1)} - \dot{v}_i^{(3)})\\
& - (b_{12}/\phi_f)\dot{w}_i
\end{aligned} \tag{A-13}$$

and

$$\begin{aligned}
\sigma_{ij,j}^{(3)} = {} & [\rho_{13} + (1 - I)\rho_{23}]\dot{v}_i^{(1)} + (\rho_{33} + I\rho_{23})\dot{v}_i^{(3)}\\
& + (\rho_{23}/\phi_f)\ddot{w}_i + (b_{13} + I b_{23})(\dot{v}_i^{(1)} - \dot{v}_i^{(3)})\\
& - (b_{23}/\phi_f)\dot{w}_i.
\end{aligned} \tag{A-14}$$

The second equation (A-1) is equivalent to

$$-p_{f,i} = \rho_{w1}\dot{v}_i^{(1)} + \rho_{w3}\dot{v}_i^{(3)} + \psi\ddot{w}_i + \left(\frac{\eta_f}{\kappa_s}\right)\dot{w}_i^{(1)} + \left(\frac{\eta_f}{\kappa_i}\right)\dot{w}_i^{(3)}, \tag{A-15}$$

where p_f is fluid pressure. Equation A-15 can be rewritten as

$$\begin{aligned}
-p_{f,i} = {} & \rho_{w1}\dot{v}_i^{(1)} + \rho_{w3}\dot{v}_i^{(3)} + \psi\ddot{w}_i\\
& + \left(\frac{\eta_f}{\kappa}\right)\left[\dot{w}_i + \phi_f\left(I - \frac{\kappa}{\kappa_i}\right)(\dot{v}_i^{(3)} - \dot{v}_i^{(1)})\right],
\end{aligned} \tag{A-16}$$

where

$$\sigma^{(2)} = -\phi_f p_f, \tag{A-17}$$

$$\begin{aligned}
\rho_{w1} &= \rho_f [I(1 - a_{21}) + a_{23}(1 - I)],\\
\rho_{w3} &= \rho_f - \rho_{w1},\\
\psi &= \rho_f (a_{21} + a_{23} - 1)/\phi_w,
\end{aligned} \tag{A-18}$$

and

$$\kappa = \frac{\kappa_s \kappa_h}{\kappa_s + \kappa_h} \tag{A-19}$$

is the average permeability.

Let us define the stress of the composite as

$$\sigma_{ij} = \sigma_{ij}^{(1)} + \sigma_{ij}^{(3)} - \phi_f p_f \delta_{ij}. \tag{A-20}$$

Its divergence can be obtained from equations A-13, A-14, A-16, and A-17, giving

$$\begin{aligned}
\sigma_{ij,j} = {} & (1 - I)[(1 - \phi_f)\rho_s + \rho_f \phi_f]\dot{v}_i^{(1)}\\
& + I[(1 - \phi_f)\rho_h + \rho_f \phi_f]\dot{v}_i^{(3)} + \rho_f \ddot{w}_i.
\end{aligned} \tag{A-21}$$

If the rock and ice matrices move in phase and have similar properties, $v_i^{(3)} = v_i^{(1)}$, and equations A-16 and A-21 reduce to Biot's equations.

Stress-strain relations

Assuming spatially constant porosity, the constitutive equations are

$$\sigma_{ij}^{(1)} = (K_1\theta_1 + C_{12}\theta_2 + C_{13}\theta_3)\delta_{ij} + 2\mu_1 d_{ij}^{(1)} + \mu_{13} d_{ij}^{(3)},$$
$$\sigma^{(2)} = C_{12}\theta_1 + K_2\theta_2 + C_{23}\theta_3,$$
$$\sigma_{ij}^{(3)} = (K_3\theta_3 + C_{23}\theta_2 + C_{13}\theta_1)\delta_{ij} + 2\mu_3 d_{ij}^{(3)} + \mu_{13} d_{ij}^{(1)}, \quad \text{(A-22)}$$

where

$$\theta_m = \varepsilon_{ii}^{(m)},$$
$$d_{ij}^{(m)} = \varepsilon_{ij}^{(m)} - \frac{1}{3}\delta_{ij}\theta_m,$$
$$\varepsilon_{ii}^{(m)} = \frac{1}{2}(u_{i,j}^{(m)} + u_{j,i}^{(m)}),\ m = 1, 3. \quad \text{(A-23)}$$

The coupling moduli are

$$C_{12} = (1 - c_1)\phi_s\phi_f K_{av},$$
$$C_{13} = (1 - c_1)(1 - c_3)\phi_s\phi_h K_{av},$$
$$C_{23} = (1 - c_3)\phi_h\phi_f K_{av}, \quad \text{(A-24)}$$

where

$$K_{av} = [(1 - c_1)\phi_s/K_s + \phi_f/K_f + (1 - c_3)\phi_h/K_h]^{-1} \quad \text{(A-25)}$$

and K_s, K_h, and K_f are the moduli of grains, hydrate, and fluid, respectively.

Moreover,

$$c_1 = K_{sm}/\phi_s K_s,$$
$$c_3 = K_{hm}/\phi_h K_h, \quad \text{(A-26)}$$

where K_{sm} and K_{hm} are the bulk moduli of the rock and ice frames. It is

$$K_{hm} = K_{max}[\phi_h/(1 - \phi_s)]^{3.8}, \quad \text{(A-27)}$$

where K_{max} is the Kuster-Toksöz's modulus of the ice frame. Moreover,

$$K_1 = [(1 - c_1)\phi_s]^2 K_{av} + K_{sm},$$
$$K_2 = \phi_f^2 K_{av},$$
$$K_3 = [(1 - c_3)\phi_h]^2 K_{av} + K_{hm} \quad \text{(A-28)}$$

and

$$\mu_{11} = [(1 - g_1)\phi_s]^2\mu_{av} + \mu_{sm},$$
$$\mu_{13} = (1 - g_1)(1 - g_3)\phi_s\phi_h\mu_{av},$$
$$\mu_{33} = [(1 - g_3)\phi_h]^2\mu_{av} + \mu_{hm}, \quad \text{(A-29)}$$

where

$$\mu_{sm} = [\mu_{smKT} - \mu_{sm0}][\phi_h/(1 - \phi_s)]^{3.8} + \mu_{sm0}, \quad \text{(A-30)}$$

(Arbabi and Sahimi, 1988) is the S-wave modulus of the rock matrix, with μ_{smKT} the Kuster-Toksöz modulus and μ_{sm0} the modulus at full water saturation.

$$\mu_{hm} = \mu_{max}[\phi_h/(1 - \phi_s)]^{3.8} \quad \text{(A-31)}$$

is the modulus of the ice matrix, where μ_{max} is Kuster-Toksöz's modulus of the ice matrix, and

$$\mu_{av} = [(1 - g_1)\phi_s/\mu_s + \phi_f/i\omega\eta_f + (1 - g_3)\phi_h/\mu_h]^{-1} \quad \text{(A-32)}$$

is an average modulus.

The corresponding consolidation coefficients are

$$g_1 = \mu_{sm}/\phi_s\mu_s,$$
$$g_3 = \mu_{hm}/\phi_h\mu_h. \quad \text{(A-33)}$$

The variation of fluid content is

$$\zeta = -\text{div}\,\mathbf{w} = -\{\phi_f[u_i^{(2)} - (1 - I)u_i^{(1)} - Iu_i^{(3)}]\}_i \quad \text{(A-34)}$$

which, for constant porosity, is

$$\zeta = -\phi_f[\theta_2 - (1 - I)\theta_1 - I\theta_3]. \quad \text{(A-35)}$$

Substituting ϕ_2 by $(1 - I)\theta_1 + I\theta_3 - \zeta/\phi_f$ into equation A-22 gives

$$\sigma_{ij}^{(1)} = [(K_{G1} - \alpha_1 M(1 - I)\phi_f)\theta_1 + M(\alpha_1 - (1 - I)\phi_f)(\alpha_3\theta_3 - \zeta)]\delta_{ij} + 2\mu_{11} d_{ij}^{(1)} + \mu_{13} d_{ij}^{(3)},$$
$$p_f = M(\zeta - \alpha_1\theta_1 - \alpha_3\theta_3),$$
$$\sigma_{ij}^{(3)} = [(K_{G3} - \alpha_3 MI\phi_f)\theta_3 + M(\alpha_3 - I\phi_f) \times (\alpha_1\theta_1 - \zeta)]\delta_{ij} + 2\mu_{33} d_{ij}^{(3)} + \mu_{13} d_{ij}^{(1)}, \quad \text{(A-36)}$$

where

$$\begin{aligned} K_{G1} &= K_{\rm sm} + \alpha_1^2 M, \\ K_{G3} &= K_{\rm hm} + \alpha_3^2 M, \\ M &= K_2/\phi_{\rm f}^2 = K_{\rm av}, \\ \alpha_1 &= 1 - K_{\rm sm}/K_{\rm s} - I, \\ \alpha_3 &= 1 - K_{\rm hm}/K_{\rm h} - (1 - I). \end{aligned} \tag{A-37}$$

The total stress (equation A-20) then is given by

$$\begin{aligned} \sigma_{ij} = [&(K_{G1} + \alpha_1\alpha_3 M)\theta_1 + (K_{G3} + \alpha_1\alpha_3 M)\theta_3 \\ &- M(\alpha_1 + \alpha_3)\zeta]\delta_{ij} + (2\mu_{11} + \mu_{13})d_{ij}^{(3)} + (2\mu_{33} \\ &+ \mu_{13})d_{ij}^{(1)}. \end{aligned} \tag{A-38}$$

At the isostrain state, $\theta_1 = \theta_2 = \theta_3$, implying that $\zeta = 0$, and the Gassmann modulus is

$$K_G = K_{\rm sm} + K_{\rm hm} + \alpha^2 M, \tag{A-39}$$

where

$$\alpha = \alpha_1 + \alpha_3 = 1 - K_{\rm sm}/K_{\rm s} - K_{\rm hm}/K_{\rm h}. \tag{A-40}$$

Equations A-13, A-14, A-16, and A-36 are valid for variable porosity (Carcione et al., 2003).

Seismic velocities

The three P-wave velocities are

$$V_{{\rm P}i} = [{\rm Re}(\sqrt{\Lambda_i})]^{-1},\ i = 1, 2, 3, \tag{A-41}$$

where Re indicates the real part and Λ_i are eigenvalues, solutions of

$$\begin{aligned} A\Lambda^3 - [&\rho_{11}B + \rho_{22}C + \rho_{33}D - 2E + 2F]\Lambda^2 \\ &+ [bR_{11} + cR_{22} + dR_{33} - 2e + 2f]\Lambda - a = 0. \end{aligned} \tag{A-42}$$

The velocities of the two S-waves are

$$V_{{\rm S}i} = [{\rm Re}(\sqrt{\boldsymbol{\Omega}_i})]^{-1},\ i = 1, 2, \tag{A-43}$$

where Ω_i are solutions of

$$\begin{aligned} \boldsymbol{\Omega}^2\rho_{22}(\mu_{11}\mu_{33} - \mu_{13}) - \boldsymbol{\Omega}(&\mu_{11}b + \mu_{33}d - 2\mu_{13}\rho_{13}\rho_{22} \\ &+ 2\mu_{13}\rho_{12}\rho_{23}) + a = 0. \end{aligned} \tag{A-44}$$

The coefficients are

$$\begin{aligned} A &= R_{11}R_{22}R_{33} - R_{23}^2R_{11} - R_{12}^2R_{33} - R_{13}^2R_{22} \\ &\quad + 2R_{12}R_{23}R_{13}, \\ B &= R_{22}R_{33} - R_{23}^2, \\ C &= R_{11}R_{33} - R_{13}^2, \\ D &= R_{11}R_{22} - R_{12}^2, \\ E &= R_{11}R_{23}\rho_{23} + R_{33}R_{12}\rho_{12} + R_{22}R_{13}\rho_{13}, \\ F &= R_{12}R_{13}\rho_{23} + R_{23}R_{12}\rho_{13} + R_{23}R_{13}\rho_{12}, \\ a &= \rho_{11}\rho_{22}\rho_{33} - \rho_{23}^2\rho_{11} - \rho_{12}^2\rho_{33} - \rho_{13}^2\rho_{22}, \\ b &= \rho_{22}\rho_{33} - \rho_{23}^2, \\ c &= \rho_{11}\rho_{33} - \rho_{13}^2, \\ d &= \rho_{11}\rho_{22} - \rho_{12}^2, \\ e &= \rho_{11}\rho_{23}R_{23} + \rho_{33}\rho_{12}R_{12} + \rho_{13}\rho_{22}R_{13}, \\ f &= \rho_{12}\rho_{13}R_{23} + \rho_{23}\rho_{12}R_{13} + \rho_{13}\rho_{23}R_{12}, \end{aligned}$$

$$\begin{aligned} R_{11} &= K_1 + \frac{4}{3}\mu_{11}, \\ R_{12} &= C_{12}, \\ R_{22} &= \phi_f^2 K_{\rm av}, \\ R_{23} &= C_{13} + \frac{2}{3}\mu_{13}, \\ R_{33} &= K_3 + \frac{4}{3}\mu_{33}. \end{aligned} \tag{A-45}$$

We use the theory of Santos et al. (1990a) and Santos et al. (1990b) to obtain the wave velocities of sediments partially saturated with gas and water.

Attenuation

According to experimental data, seismic attenuation is approximately linear as a function of frequency (Q is constant). Scott Blair (1949) introduces this model, and Bland (1960) and Kjartansson (1979) provide a more detailed mathematical framework. The kernel is

$$M(\omega, Q) = \left(\frac{i\omega}{\omega_0}\right),\ \lambda = \frac{1}{\pi}\tan^{-1}\left(\frac{1}{Q}\right), \tag{A-46}$$

where ω_0 is a reference frequency. To introduce attenuation, we perform the following replacement:

$$K_{\rm sm} \rightarrow K_{\rm sm}M(\omega, Q_K), \tag{A-47}$$

where

$$Q_K = \frac{K_{\rm sm}(z, p)}{K_{\rm sm}(z)}Q_0, \tag{A-48}$$

where Q_0 is a loss parameter, and $K_{sm}(z)$ is the modulus at 100% water saturation and normal fluid pressure. On the other hand, for shear waves,

$$Q_\mu = \frac{\mu_{sm}(z, p)}{\mu_{sm}(z)} Q_K, \tag{A-49}$$

and

$$\mu_{sm} \rightarrow \mu_{sm} M(\omega, Q_\mu). \tag{A-50}$$

Alternative models for suspensions are given in Urick (1948) and in McCann (1970). Our theory predicts that wave loss decreases as hydrate content increases. However, other models predict an increase of attenuation in the presence of gas hydrates (Dvorkin and Uden, 2004; Guerin and Goldberg, 2005).

Figures A-1, A-2, and A-3 show examples of 3D plots of the P- and S-wave properties as a function of saturation, effective pressure, and frequency.

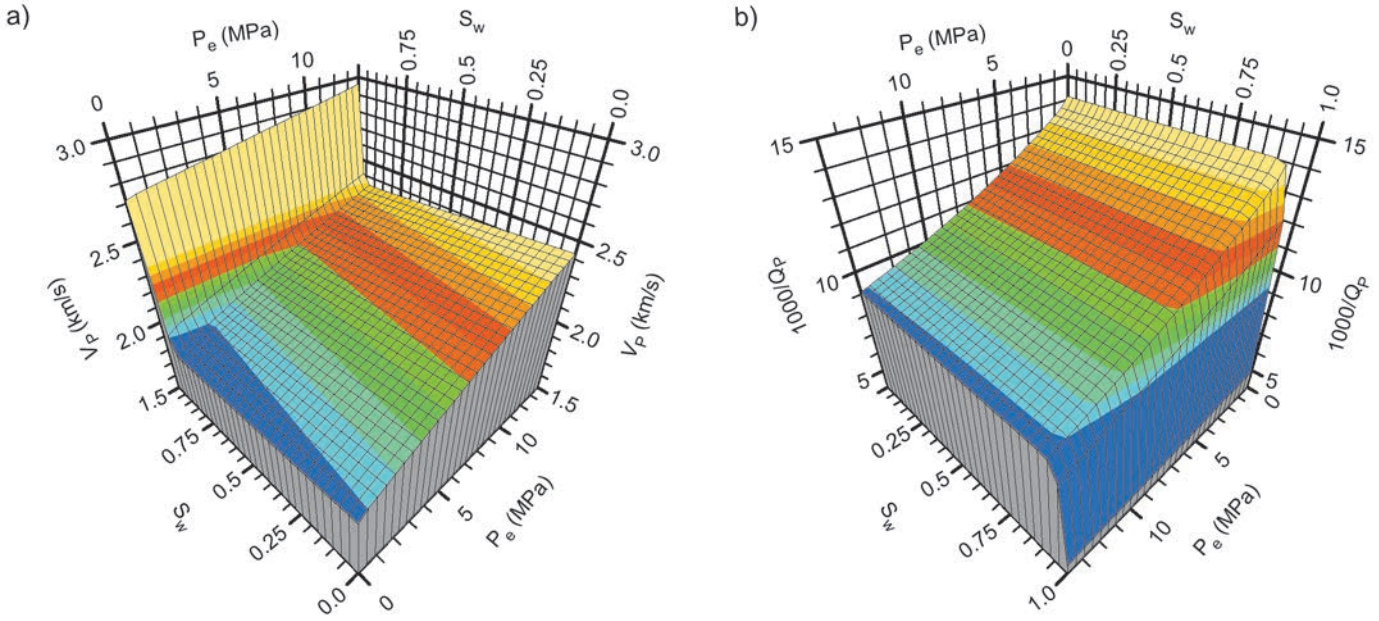

Figure A-1. (a) Compressional-wave velocity and (b) inverse quality factor versus effective pressure and water saturation. Hydrate content is 0.3, and $f = 30$ Hz. After Gei and Carcione, 2003. Used by permission.

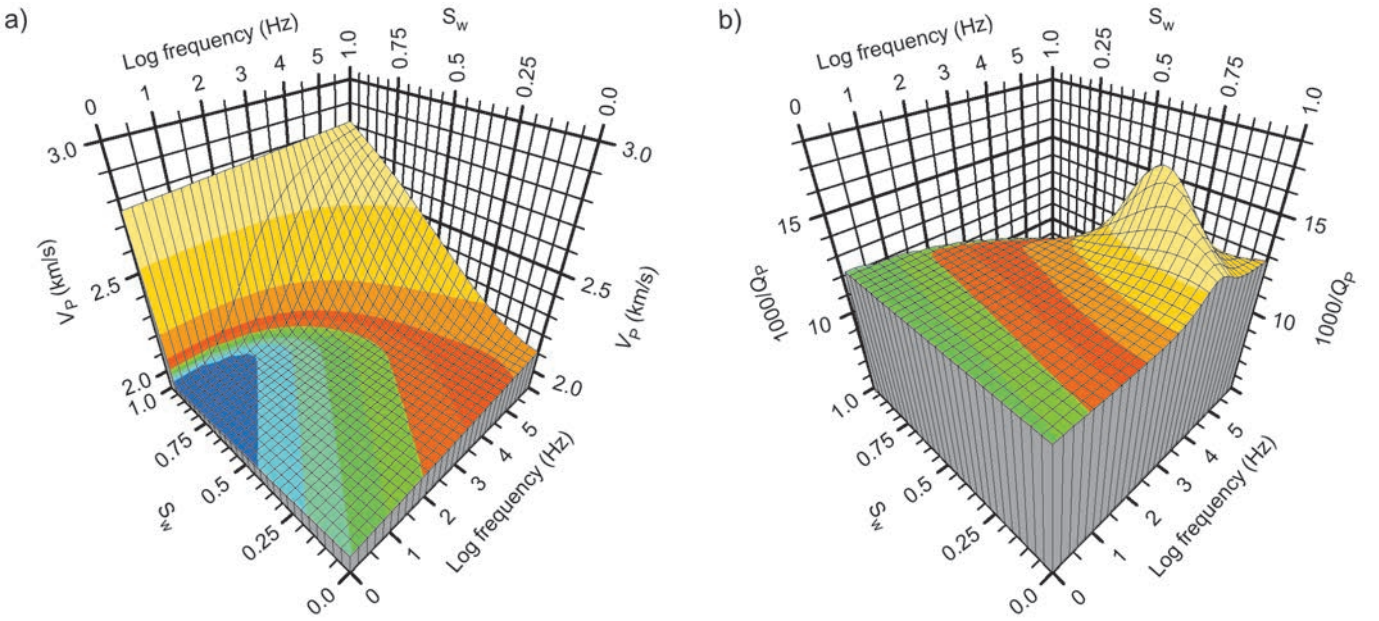

Figure A-2. (a) Compressional-wave velocity and (b) inverse quality factor versus water saturation and frequency. Hydrate content is 0.3, and differential pressure is 0.6 MPa. After Gei and Carcione, 2003. Used by permission.

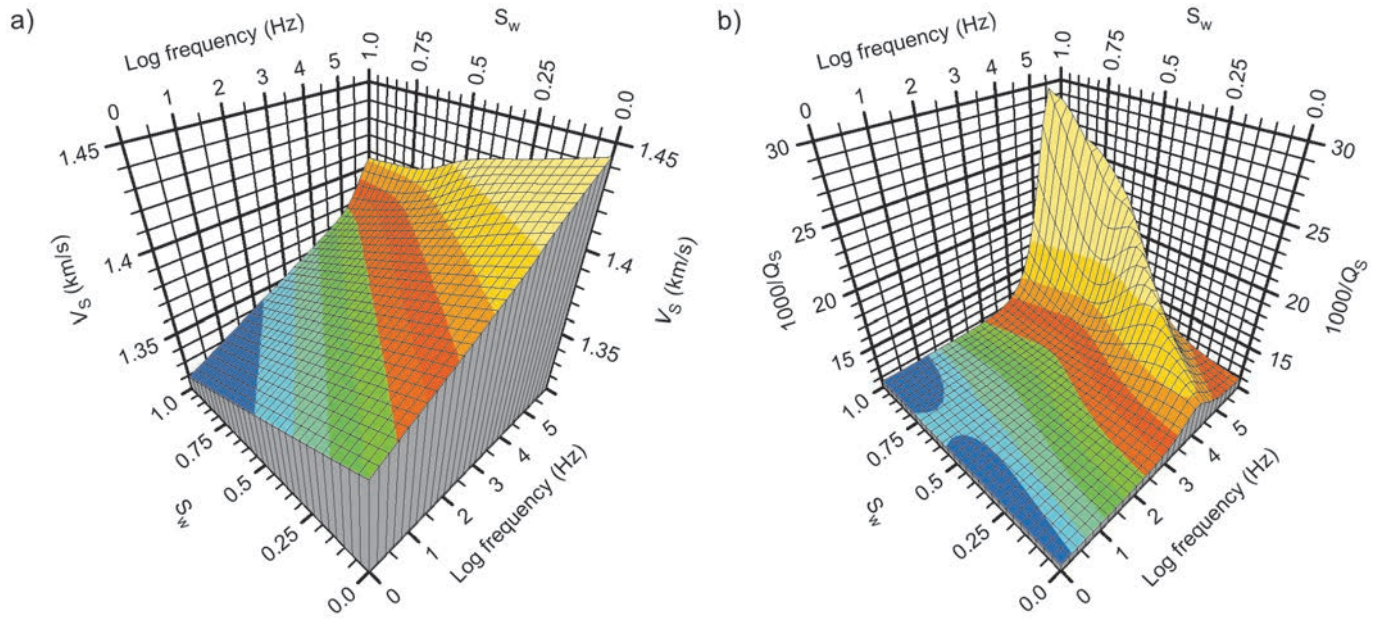

Figure A-3. (a) Shear-wave velocity and (b) inverse quality factor versus water saturation and frequency. Hydrate content is 0.3, and differential pressure is 0.6 MPa. After Gei and Carcione, 2003. Used by permission.

References

Arbabi, S., and M. Sahimi, 1988, Elastic properties of three-dimensional percolation networks with stretching and bond-bending forces: Physical Review B: Condensed Matter and Materials Physics, **38**, no. 10, 7173–7176, doi:10.1103/PhysRevB.38.7173.

Berryman, J. G., 1980, Confirmation of Biot's theory: Applied Physics Letters, **37**, no. 4, 382–384, doi:10.1063/1.91951.

Biot, M. A., 1956, Theory of propagation of elastic waves in a fluid-saturated porous solid, I: Low-frequency range: Journal of the Acoustical Society of America, **28**, no. 2, 168–178, doi:10.t1121/1.1908239.

Biot, M. A., 1962, Mechanics of deformation and acoustic propagation in porous media: Journal of Applied Physics, **33**, no. 4, 1482–1498, doi:10.1063/1.1728759.

Bland, D. R., 1960, The theory of linear viscoelasticity: Pergamon Press, Inc.

Böhm, G., G. Rossi, and A. Vesnaver, 1997, Adaptive regridding in 3-D reflection tomography: Annali di Geofisica, **40**, no. 1, 69–83.

Böhm, G., G. Rossi, and A. Vesnaver, 2002, Tomography of converted waves for sub-high velocity layers targets using OBC data: 72nd Annual International Meeting, SEG, Expanded Abstracts, 846–849.

Brie, A., F. Pampuri, A. F. Marsala, and O. Meazza, 1995, Shear sonic interpretation in gas-bearing sands: Annual Technical Conference, SPE #30595, 701–710.

Brown, K. M., 1990, The nature and hydrogeologic significance of mud diapirs and diatremes for accretionary systems: Journal of Geophysical Research, Solid Earth, **95**, no. B6, 8969–8982, doi:10.1029/JB095iB06p08969.

Bünz, S., and J. Mienert, 2004, Acoustic imaging of gas hydrate and free gas at the Storegga Slide: Journal of Geophysical Research, Solid Earth, **109**, no. B4, B04102, doi:10.1029/2003JB002863.

Cadoret, T., D. Marion, and B. Zinszner, 1995, Influence of frequency and fluid distribution on elastic wave velocities in partially saturated limestones: Journal of Geophysical Research, Solid Earth, **100**, no. B6, 9789–9803, doi:10.1029/95JB00757.

Carcione, J. M., 1997, Reflection and transmission of *qP-qS* plane waves at a plane boundary between viscoelastic transversely isotropic media: Geophysical Journal International, **129**, no. 3, 669–680, doi:10.1111/j.1365-246X.1997.tb04502.x.

Carcione, J. M., 2007, Wave fields in real media: Wave propagation in anisotropic, anelastic, porous and electromagnetic media: Handbook of geophysical exploration, 2nd ed., v. 38: Elsevier.

Carcione, J. M., F. Cavallini, F. Mainardi, and A. Hanyga, 2002, Time-domain seismic modeling of constant *Q*-wave propagation using fractional derivatives: Pure and Applied Geophysics, **159**, no. 7, 1719–1736, doi:10.1007/s00024-002-8705-z.

Carcione, J. M., and D. Gei, 2004, Gas hydrate concentration estimated from P- and S-wave velocities at the Mallik 2L-38 research well, Mackenzie Delta, Canada: Journal of Applied Geophysics, **56**, no. 1, 73–78, doi:10.1016/j.jappgeo.2004.04.001.

Carcione, J. M., D. Gei, G. Rossi, and G. Madrussani, 2005a, Estimation of gas-hydrate concentration and free-gas saturation at the Norwegian-Svalbard continental margin: Geophysical Prospecting, **53**, no. 6, 803–810, doi:10.1111/j.1365-2478.2005.00502.x.

Carcione, J. M., and H. B. Helle, 1999, Numerical solution of the poroviscoelastic wave equation on a staggered mesh: Journal of Computational Physics, **154**, no. 2, 520–527, doi:10.1006/jcph.1999.6321.

Carcione, J. M., H. B. Helle, J. E. Santos, and C. L. Ravazzoli, 2005b, A constitutive equation and generalized Gassmann modulus for multimineral porous media: Geophysics, **70**, no. 2, N17–N26, doi:10.1190/1.1897035.

Carcione, J. M., and S. Picotti, 2006, P-wave seismic attenuation by slow-wave diffusion: Effects of inhomogeneous rock properties: Geophysics, **71**, no. 3, O1–O8, doi:10.1190/1.2194512.

Carcione, J. M., J. E. Santos, C. L. Ravazzoli, and H. B. Helle, 2003, Wave simulation in partially frozen porous media with fractal freezing conditions: Journal of Applied Physics, **94**, no. 12, 7839–7847, doi:10.1063/1.1606861.

Carcione, J. M., and G. Seriani, 2001, Wave simulation in frozen sediments: Journal of Computational Physics, **170**, no. 2, 1–20, doi:10.1006/jcph.2001.6756.

Carcione, J. M., and U. Tinivella, 2000, Bottom-simulating reflectors: Seismic velocities and AVO effects: Geophysics, **65**, 54–67; Errata, 2001, **66**, 984.

Chand, S., T. A. Minshull, D. Gei, and J. M. Carcione, 2004, Elastic velocity models for gas-hydrate-bearing sediments — A comparison: Geophysical Journal International, **159**, no. 2, 573–590, doi:10.1111/j.1365-246X.2004.02387.x.

Collett, T. S., R. E. Lewis, S. R. Dallimore, M. W. Lee, T. H. Mroz, and T. Uchida, 1999, Detailed evaluation of gas hydrate reservoir properties using JAPEX/JNOC/GSC Mallik 2L-38 gas hydrate research well downhole well-log displays, *in* S. R. Dallimore, T. Uchida, and T. S. Collett, eds., Scientific results from JAPEX/JNOC/GSC Mallik 2L-38 gas hydrate research well, Mackenzie Delta, Northwest Territories, Canada: Geological Survey of Canada Bulletin, **544**, 295–311.

Dvorkin, J., and R. Uden, 2004, Seismic wave attenuation in a methane hydrate reservoir: The Leading Edge, **23**, no. 8, 730–734, doi:10.1190/1.1786892.

Ecker, C., J. Dvorkin, and A. Nur, 1998, Sediments with gas hydrates: Internal structure from seismic AVO: Geophysics, **63**, 1659–1669, doi:10.1190/1.1444462.

Ecker, C., J. Dvorkin, and A. Nur, 2000, Estimating the amount of gas hydrate and free gas from marine seismic data: Geophysics, **65**, 565–573, doi:10.1190/1.1444752.

Gassmann, F., 1951, Über die Elastizität poröser Medien: Vierteljahrsschrift der Naturforschenden Gesellschaft in Zürich, **96**, 1–23.

Gei, D., and J. M. Carcione, 2003, Acoustic properties of sediments saturated with gas hydrate, free gas and water: Geophysical Prospecting, **51**, no. 2, 141–158, doi:10.1046/j.1365-2478.2003.00359.x.

Guerin, G., and D. Goldberg, 2002, Sonic waveform attenuation in gas hydrate-bearing sediments from the Mallik 2L-38 research well, Mackenzie Delta, Canada: Journal of Geophysical Research, Solid Earth, **107**, no. B5, 2088, EPM X-1–EPM X-11, doi:10.1029/2001JB000556.

Guerin, G., and D. Goldberg, 2005, Modeling of acoustic wave dissipation in gas hydrate-bearing sediments: Geochemistry, Geophysics, Geosystems (G^3), **6**, no. 7, Q07010, doi:10.1029/2005GC000918.

Hamilton, E. L., 1976, Variation of density and porosity with depth in deep-sea sediments: Journal of Sedimentary Petrology, **46**, 280–300.

Hamilton, E. L., 1979, V_P/V_S and Poisson's ratios in marine sediments and rocks: Journal of the Acoustical Society of America, **66**, no. 4, 1093–1101, doi:10.1121/1.383344.

Helgerud, M. B., J. Dvorkin, A. Nur, A. Sakai, and T. Collett, 1999, Elastic-wave velocity in marine sediments with gas hydrates: Effective medium modeling: Geophysical Research Letters, **26**, no. 13, 2021–2024, doi:10.1029/1999GL900421.

Jakobsen, M., J. A. Hudson, T. A. Minshull, and S. C. Singh, 2000, Elastic properties of hydrate-bearing sediments using effective-medium theory: Journal of Geophysical Research, Solid Earth, **105**, B1, 561–577, doi:10.1029/1999JB900190.

Jansen, E., M. E. Raymo, P. Blum, and the Shipboard Scientific Party, Ocean Drilling Program, Leg 162, Site 986, 1996, Proceedings of the Ocean Drilling Program, Initial Report, v. 162.

Johnson, D. L., J. Koplik, and R. Dashen, 1987, Theory of dynamic permeability and tortuosity in fluid-saturated porous media: Journal of Fluid Mechanics, **176**, no. 1, 379–402, doi:10.1017/S0022112087000727.

Katsube, T. J., S. R. Dallimore, T. Uchida, K. A. Jenner, T. S. Collett, and S. Connell, 1999, Petrophysical

environment of sediments hosting gas hydrate, JAPEX/JNOC/GSC Mallik 2L-38 gas hydrate research well: Geological Survey of Canada Bulletin, **544**, 109–124.

Kjartansson, E., 1979, Constant *Q*-wave propagation and attenuation: Journal of Geophysical Research, Solid Earth, **84**, no. B9, 4737–4748, doi:10.1029/JB084iB09p04737.

Leclaire, P., F. Cohen-Ténoudji, and J. Aguirre-Puente, 1994, Extension of Biot's theory of wave propagation to frozen porous media: Journal of the Acoustical Society of America, **96**, no. 6, 3753–3768, doi:10.1121/1.411336.

Leclaire, P., F. Cohen-Ténoudji, and J. Aguirre-Puente, 1995, Observation of two longitudinal and two transverse waves in a frozen porous medium: Journal of the Acoustical Society of America, **97**, no. 4, 2052–2055, doi:10.1121/1.411997.

Lee, M. V., D. R. Hutchinson, T. S. Collett, and W. P. Dillon, 1996, Seismic velocities for hydrate-bearing sediments using weighted equation: Journal of Geophysical Research, Solid Earth, **101**, no. B9, 20347–20358, doi:10.1029/96JB01886.

Lee, M. Q. W., 2006, Is amplitude loss of sonic waveforms due to intrinsic attenuation or source coupling of the medium?: USGS Scientific Investigation Report 2006–5120.

Lundin, E., and A. G. Doré, 2002, Mid-Cenozoic postbreakup deformation in the passive margins bordering the Norwegian-Greenland Sea: Marine and Petroleum Geology, **19**, no. 1, 79–93, doi:10.1016/S0264-8172(01)00046-0.

Matsushima, J., 2006, Seismic wave attenuation in methane hydrate-bearing sediments: Vertical seismic profiling data from the Nankai trough exploratory well, offshore Tokai, central Japan: Journal of Geophysical Research, Solid Earth, **111**, B10101, doi:10.1029/2005JB004031.

McCann, C., 1970, Compressional wave attenuation in concentrated clay suspensions: Acustica, **22**, 352–356.

Miyairi, M., K. Akihisa, T. Uchida, T. S. Collett, and S. R. Dallimore, 1999, Well-log interpretation of gas-hydrate-bearing formations in the JAPEX/JNOC/GSC Mallik 2L-38 gas hydrate research well, *in* S. R. Dallimore, T. Uchida, and T. S. Collett, eds., Scientific results from JAPEX/JNOC/GSC Mallik 2L-38 gas hydrate research well, Mackenzie Delta, Northwest Territories, Canada: Geological Survey of Canada Bulletin, **544**, 281–293.

Ojha, M., and K. Sain, 2007, Seismic velocities and quantification of gas-hydrates from AVA modeling in the western continental margin of India: Marine Geophysical Research, **28**, no. 2, 101–107, doi:10.1007/s11001-007-9017-6.

Pecher, I. A., C. R. Ranero, R. Von Huene, T. A. Minshull, and S. C. Singh, 1998, The nature and distribution of bottom simulating reflectors at the Costa Rican convergent margin: Geophysical Journal International, **133**, no. 2, 219–229, doi:10.1046/j.1365-246X.1998.00472.x.

Picotti, S., and J. M. Carcione, 2006, Estimating seismic attenuation (Q) in the presence of random noise: Journal of Seismic Exploration, **15**, no. 2, 165–181.

Priest, J. A., A. I. Best, and C. R. I. Clayton, 2006, Attenuation of seismic waves in methane gas hydrate-bearing sand: Geophysical Journal International, **164**, no. 1, 149–159, doi:10.1111/j.1365-246X.2005.02831.x.

Quan, Y., and J. M. Harris, 1997, Seismic attenuation tomography using the frequency shift method: Geophysics, **62**, 895–905, doi:10.1190/1.1444197.

Rossi, G., P. Corubolo, G. Böhm, E. Ceragioli, P. Dell'Aversana, S. Morandi, F. Poletto, and A. Vesnaver, 2001, Joint 3-D inversion of SWD and surface seismic data: First Break, **19**, no. 8, 453–459, doi:10.1046/j.0263-5046.2001.00198.x.

Rossi, G., D. Gei, G. Böhm, G. Madrussani, and J. M. Carcione, 2007, Attenuation tomography: An application to gas-hydrate and free-gas detection: Geophysical Prospecting, **55**, no. 5, 655–669, doi:10.1111/j.1365-2478.2007.00646.x.

Rossi, G., G. Madrussani, D. Gei, G. Böhm, and A. Camerlenghi, 2005, Velocity and attenuation 3D tomography for gas-hydrates studies: The NW offshore Svalbard case: Proceedings of the Fifth International Conference on Gas Hydrates, Trondheim, Norway, June 13–16, 677–682.

Rossi, G., and A. Vesnaver, 2001, Joint 3D traveltime inversion of P, S and converted waves: Journal of Computational Acoustics, **9**, no. 4, 1407–1416, doi:10.1016/S028-396X(01)00149-2.

Ruan, A., and X. Li, 2006, Analysis of AVA method for gas hydrate study: Journal of Marine Sciences, **24**, no. 4, 22–28, doi:cnki:ISSN:1001-909X.0.2006-04-000.

Santos, J. E., J. M. Corberó, and J. Douglas Jr., 1990a, Static and dynamic behavior of a porous solid saturated by a two-phase fluid: Journal of the Acoustical Society of America, **87**, no. 4, 1428–1438, doi:10.1121/1.399439.

Santos, J. E., J. Douglas Jr., J. Corberó, and O. M. Lovera, 1990b, A model for wave propagation in a porous medium saturated by a two-phase fluid: Journal of the Acoustical Society of America, **87**, no. 4, 1439–1448, doi:10.1121/1.399440.

Scott Blair, G. W., 1949, A survey of general and applied rheology: Pitman.

Tinivella, U., 1999, A method for estimating gas hydrate and free gas concentrations in marine sediments: Bollettino di Geofisica Teorica ed Applicata, **40**, no. 1, 19–30.

Tinivella, U., 2002, The seismic response to overpressure versus gas hydrate and free gas concentration: Journal of Seismic Exploration, **11**, 283–305.

Tinivella, U., and F. Accaino, 2000, Compressional velocity structure and Poisson's ratio in marine sediments with gas hydrate and free gas by inversion of reflected and refracted seismic data (South Shetland Islands, Antarctica): Marine Geology, **164**, no. 1–2, 13–27, doi:10.1016/S0025-3227(99)00123-1.

Tinivella, U., F. Accaino, and A. Camerlenghi, 2002, Gas hydrate and free gas distribution from inversion of seismic data on the South Shetland margin (Antarctica): Marine Geophysical Research, **23**, 109–123.

Tinivella, U., F. Accaino, and B. Della Vedova, 2008, Gas hydrates and active mud volcanism on the South Shetland continental margin, Antarctic Peninsula: Geo-Marine Letters, **28**, no. 2, 97–106, doi:10.1007/s00367-007-0093-z.

Tinivella, U., M. Giustiniani, and D. Accettella, 2011, BSR versus climate change and slides: Journal of Geological Research, article 390547, doi:10.1155/2011/390547.

Tinivella, U., E. Lodolo, A. Camerlenghi, and G. Böhm, 1998, Seismic tomography study of a bottom simulating reflector off the South Shetland Islands (Antarctica), *in* J. P. Henriet and J. Mienert, eds., Gas hydrates: Relevance to world margin stability and climate change: Geological Society [London] Special Publications 137, 141–151.

Tinivella, U., M. F. Loreto, and F. Accaino, 2009, Regional versus detailed velocity analysis to quantify hydrate and free gas in marine sediments: The South Shetland Margin case study, *in* D. Long, M. A. Lovell, J. G. Rees, and C. A. Rochelle, eds., Sediment-hosted gas hydrates: New insights on natural and synthetic systems. Geological Society [London] Special Publications 319, 103–119.

Urick, R. J., 1948, Absorption of sound in suspensions of irregular particles: Journal of the Acoustical Society of America, **20**, no. 3, 283–289, doi:10.1121/1.1906373.

Vanneste, M., S. Guidard, and J. Mienert, 2005, Bottom-simulating reflections and geothermal gradients across the western Svalbard margin: Terra Nova, **17**, no. 6, 510–516, doi:10.1111/j.1365-3121.2005.00643.x.

Vanneste, M., J. Mienert, S. Guidard, S., and Hydratech-INGGAS partners, 2002, "Arctic" gas hydrates offshore western Svalbard, Norway: Proceedings of the Fourth International Conference on Gas Hydrates, Yokohama, May 19–23, 222–227.

Vesnaver, A., 1996, The contribution of reflected, refracted and transmitted waves to seismic tomography: A tutorial: First Break, **14**, no. 5, 159–168.

Vesnaver, A., and G. Böhm, 2000, Staggered or adapted grids for seismic tomography?: The Leading Edge, **19**, no. 9, 944–950, doi:10.1190/1.1438762.

Walia, R., Y. Mi, R. D. Hyndman, and A. Sakai, 1999, Vertical seismic profile (VSP) in the JAPEX/JNOC/GSC Mallik 2L-38 gas hydrate research well, *in* S. R. Dallimore, T. Uchida, and T. S. Collett, eds., Scientific results from JAPEX/JNOC/GSC Mallik 2L-38 gas hydrate research well, Mackenzie Delta, Northwest Territories, Canada: Geological Survey of Canada Bulletin, **544**, 341–355.

Westbrook, G. K., S. Buenz, A. Camerlenghi, J. M. Carcione, S. Chand, S. Dean, J.-P. Foucher, E. Flueh, D. Gei, R. Haacke, F. Klingenhoefer, C. Long, G. Madrussani, J. Mienert, T. A. Minshull, H. Nouzé, S. Peacock, G. Rossi, E. Roux, T. Reston, M. Vanneste, and M. Zillmer, 2005, Measurements of P- and S-wave velocities, and the estimation of hydrate concentration at sites in the continental margin of Svalbard and the Storegga region of Norway: Proceedings of the Fifth International Conference on Gas Hydrates, Trondheim, Norway, paper 3004, 726–735.

Westbrook, G. K., S. Chand, G. Rossi, C. Long, S. Bünz, A. Camerlenghi, J. M. Carcione, S. Dean, J.-P. Foucher, E. Flueh, D. Gei, R. R. Haacke, G. Madrussani, J. Mienert, T. A. Minshull, H. Nouzé, S. Peacock, T. J. Reston, M. Vanneste, and M. Zillmer, 2008, Estimation of gas-hydrate concentration from multi-component seismic data at sites on the continental margins of NW Svalbard and the Storegga region of Norway: Marine and Petroleum Geology, **25**, no. 8, 744–758, doi:10.1016/j.marpetgeo.2008.02.003.

Wood, W. T., W. S. Holbrook, and H. Hoskins, 2000, In situ measurements of P-wave attenuation in the methane hydrate- and gas-bearing sediments of the Blake Ridge, *in* C. K. Paull, R. Matsumoto, P. J. Wallace, and W. P. Dillon, eds., Proceedings of the Ocean Drilling Program, Scientific Results, **164**, 265–272.

Wright, J. F., A. E. Taylor, S. R. Dallimore, and F. M. Nixon, 1999, Estimating in situ gas hydrate saturation from core temperature observations, JAPEX/JNOC/GSC Mallik 2L-38 gas hydrate research well, *in* S. R.

Dallimore, T. Uchida, and T. S. Collett, eds., Scientific results from JAPEX/JNOC/GSC Mallik 2L-38 gas hydrate research well, Mackenzie Delta, Northwest Territories, Canada: Geological Survey of Canada Bulletin, **544**, 101–108.

Zucca, J. J., L. J. Hutchings, and P. W. Kasameyer, 1994, Seismic velocity and attenuation structure of the Geysers geothermal field, California: Geothermics, **23**, no. 2, 111–126, doi:10.1016/0375-6505(94)90033-7.